MNRAS **000**, 1–19 (2017) Preprint 9 January 2018 Compiled using MNRAS LATEX style file v3.0

The connection between mass, environment and slow rotation in simulated galaxies

Claudia del P. Lagos[1,2⋆], Joop Schaye[3], Yannick Bahé[3], Jesse Van de Sande[4], Scott T. Kay[5], David Barnes[5,6], Timothy A. Davis[7], Claudio Dalla Vecchia[8,9]

[1]*International Centre for Radio Astronomy Research (ICRAR), M468, University of Western Australia, 35 Stirling Hwy, Crawley, WA 6009, Australia.*
[2]*Australian Research Council Centre of Excellence for All-sky Astrophysics (CAASTRO), 44 Rosehill Street Redfern, NSW 2016, Australia.*
[3]*Leiden Observatory, Leiden University, PO Box 9513, NL-2300 RA Leiden, the Netherlands.*
[4]*Sydney Institute for Astronomy, School of Physics A28, The University of Sydney, NSW 2006, Australia.*
[5]*Jodrell Bank Centre for Astrophysics, School of Physics and Astronomy, The University of Manchester, Manchester M13 9PL, UK.*
[6]*Department of Physics, Kavli Institute for Astrophysics and Space Research, Massachusetts Institute of Technology, Cambridge, MA 02139, USA.*
[7]*Department of Physics and Astronomy, Cardiff University, Queens Buildings, The Parade, Cardiff CF24 3AA, United Kingdom.*
[8]*Instituto de Astrofísica de Canarias, C/Vía Láctea s/n, E-38205 La Laguna, Tenerife, Spain.*
[9]*Departamento de Astrofísica, Universidad de La Laguna, Av. del Astroftsico Francisco Sánchez s/n, E-38206 La Laguna, Tenerife, Spain.*

9 January 2018

ABSTRACT

Recent observational results from integral field spectroscopic (IFS) surveys indicate that the fraction of galaxies that are slow rotators, $F_{\rm SR}$, depends primarily on stellar mass, with no significant dependence on environment. We investigate these trends and the formation paths of slow rotators using the EAGLE and HYDRANGEA hydro-dynamical simulation suites. EAGLE consists of several cosmological boxes of volumes up to $(100\,{\rm Mpc})^3$, while HYDRANGEA consists of 24 cosmological zoom-in simulations of galaxy clusters and their large scale environment. Together they provide a statistically significant sample in the stellar mass range of interest, $10^{9.5}\,{\rm M}_\odot - 10^{12}\,{\rm M}_\odot$, of 16,358 galaxies. We construct IFS-like cubes and measure stellar spin parameters, $\lambda_{\rm R}$, and ellipticities, allowing us to classify galaxies into slow and fast rotators as in observations. The simulated galaxies display a primary dependence of $F_{\rm SR}$ on stellar mass, with a weak dependence on environment. At fixed stellar mass, satellite galaxies are more likely to be slow rotators than centrals. In addition, $F_{\rm SR}$ shows a dependence on halo mass at fixed stellar mass for central galaxies, while no such trend is seen for satellites. We find that $\approx 70\%$ of slow rotators at $z = 0$ have experienced at least one merger with mass ratio $\geqslant 0.1$, with dry major mergers being at least twice more common than minor and wet major mergers in this population. Individual dry mergers tend to decrease $\lambda_{\rm R}$, while wet mergers mostly increase it. However, 30% of slow rotators at $z = 0$ have not experienced mergers, and those inhabit halos with median spins twice smaller than the halos hosting the rest of the slow rotators. Thus, although the formation paths of slow rotators can be varied, dry major mergers and/or halos with small spins dominate.

Key words: galaxies: formation - galaxies: evolution - galaxies: kinematics and dynamics - galaxies: structure

1 INTRODUCTION

Integral field spectroscopy (IFS) is opening a new window for exploring galaxy formation and evolution. Many recent surveys, such as ATLAS$^{\rm 3D}$ (Cappellari et al. 2011), SAMI (Croom et al. 2012; Bryant et al. 2015), CALIFA (Sánchez et al. 2012), MASSIVE (Ma et al. 2014) and MaNGA (Bundy et al. 2015) are exploring how the resolved kinematics of the stars and ionised gas relate to global galaxy properties, such as stellar mass, colour, star formation rate (SFR) and environment, among others. The most revolutionizing aspect of these surveys is that due to their significant volumes, they are able to observe many hundreds to many thousands galaxies spanning a very wide dynamic range in mass and environment. This enables the galaxy population to be dissected into many properties, but most significantly into stellar and environment, which are thought to be primary drivers in the evolution of galaxies (e.g. Peng et al. 2010).

One of the most prominent early examples of the success of IFS surveys was the pioneering work of the SAURON (Bacon et al. 2001) and ATLAS$^{\rm 3D}$ (Cappellari et al. 2011) surveys, comprised of 260 early-type galaxies in total. These surveys showed that the stellar kinematics and distributions of stars are not strongly correlated in early-types, and thus that morphology is not necessarily a good indicator of the dynamics of galaxies (Krajnović et al. 2013).

⋆ E-mail: claudia.lagos@icrar.org

Based on these surveys, Emsellem et al. (2007, 2011) coined the terms *slow* and *fast* rotators, and proposed the $\lambda_{\rm R}$ parameter, which measures how rotationally or dispersion-dominated a galaxy is, as a new, improved scheme to classify galaxies. The most significant trend found by Emsellem et al. (2011) and extended recently to higher stellar masses by Veale et al. (2017b), is that the fraction of slow rotators increases steeply with stellar mass and towards denser environments, and that the vast majority of S0 galaxies are fast rotators.

Recent surveys spanning much larger volumes have been able to revisit this issue including the trends with environment. Brough et al. (2017), Veale et al. (2017b) and Greene et al. (2017) using the SAMI, MASSIVE and MaNGA surveys, respectively, found that the fraction of slow rotators depends strongly on stellar mass, with a very weak or no dependence on environment once stellar mass is controlled for (see Houghton et al. 2013; D'Eugenio et al. 2013 for earlier studies on cluster regions). They found that the original environmental dependence reported in ATLAS$^{\rm 3D}$ (Emsellem et al. 2011) was fully accounted for by massive galaxies preferentially living in denser environments. Interestingly, the three surveys reached the same conclusion despite the very different environments and mass ranges studied. Brough et al. (2017) focused on cluster galaxies only, while Greene et al. (2017) covered a much wider halo mass range, $M_{\rm halo} = \left(< 10^{12}\,{\rm M}_{\odot}, 10^{15}\,{\rm M}_{\odot}\right)$. Veale et al. (2017b) on the other hand make no environmental selection, but only study galaxies with stellar masses $\gtrsim 10^{11}\,{\rm M}_{\odot}$. Note, however, that Greene et al. (2017) observed a weak trend for satellite galaxies to display a slightly higher frequency of slow rotation than centrals at fixed stellar mass, but this trend is not significant. Thus, the question of whether there is an environmental effect on the incidence of slow rotation or not, and in which regimes it is more likely to be significant, remains unanswered.

The early results from SAURON and ATLAS$^{\rm 3D}$ prompted a wealth of simulations and theoretical work. Jesseit et al. (2009), Bois et al. (2011) and Naab et al. (2014), based on simulations of modest numbers of galaxies, found that the formation paths of slow and fast rotators can be highly varied. Naab et al. (2014) showed that slow rotators could be formed as a result of wet **or dry** major mergers, or by dry minor mergers. In the case of wet mergers, the remnant can be either a fast or a slow rotators, or even a disk (e.g. Springel 2000; Cox et al. 2006; Robertson et al. 2006; Johansson et al. 2009; Di Matteo et al. 2009; Peirani et al. 2010; Lotz et al. 2010; Naab et al. 2014; Moreno et al. 2015). Sparre & Springel (2017), however, found that galaxy remnants of major mergers can easily evolve into star-forming disk galaxies unless sufficiently strong feedback is present to prevent the disk regrowth. Similarly, Moster et al. (2011) concluded that even a dry merger remnant can become a fast rotator if the surrounding gaseous halo continues to cool down, fuelling the central galaxy and leading to disk regrowth. **Naab et al. (2014) and Li et al. (2018) show that the shapes and the velocity anisotropies of galaxies can provide unique clues that may help disentangle the merger history of galaxies.**

Although valuable insight can be gained from the idealised and cosmological zoom-in simulations above, they struggle to shed light into the effect of environment and in having an unbiased representation of different formation pathways. The latter comes naturally from large, cosmological hydrodynamical simulations, which have the ability to simultaneously follow the evolution of tens of thousands of galaxies in a very wide range of environments. Recently, there has been a major breakthrough in the capability of cosmological hydrodynamical simulations to produce realistic galaxy populations. This has been achieved thanks to improved subgrid models for unresolved feedback processes, the calibration of subgrid feedback parameters to match key observables, and the ability to run large cosmological volumes with sub-kpc resolution. Examples of these simulations include EAGLE (Schaye et al. 2015), Illustris (Vogelsberger et al. 2014) and its successor Illustris-TNG (Pillepich et al. 2017), and Horizon-AGN (Dubois et al. 2014).

The simulations above reproduce, with various degrees of success, the morphological diversity of galaxies observed in the local Universe, the galaxy colour bimodality, the SFR-stellar mass relation, the stellar mass function and the cosmic SFR density evolution (e.g. Furlong et al. 2015; Genel et al. 2014; Trayford et al. 2015, 2016; Snyder et al. 2015; Dubois et al. 2016; Nelson et al. 2017). Recently, Penoyre et al. (2017) analysed the formation path of thousands of elliptical galaxies in Illustris and concluded that major mergers were the most important formation path of slow rotators. Surprisingly, Penoyre et al. (2017) found no significant difference between the effect of dry vs. wet mergers on the spin of galaxies, in contradiction with the work of Naab et al. (2014) on cosmological zooms. **Li et al. (2018), also on the Illustris simulation, showed that the orbital parameters of the merger can affect the rotation of the remnant galaxy, with circular orbits preferentially producing fast rotators (see also Lagos et al. 2018).**

In this paper we use the EAGLE and HYDRANGEA simulations with the aim of exploring how the frequency of slow rotators depend on mass and environment. EAGLE simulated a box of $100({\rm cMpc})^3$, while HYDRANGEA is a suite of 24 cosmological zoom-in simulations of galaxy clusters and their environments (Bahé et al. 2017), which is part of the larger Cluster-EAGLE project (Barnes et al. 2017). The latter consists of 30 galaxy clusters (6 more than HYDRANGEA). The advantage of using HYDRANGEA here is that it resolves a larger Lagrangian region of $10\,{\rm r}_{200}$ for each cluster (as oppose to $5\,{\rm r}_{200}$ in Cluster-EAGLE), allowing us to study groups around clusters. Together EAGLE and HYDRANGEA span the halo mass range $10^{11}\,{\rm M}_{\odot} - 10^{15.3}\,{\rm M}_{\odot}$ and provide large statistics. Given this wide dynamic range, we expect our simulations to be able to reveal an environmental dependence of the fraction of slow rotators if any is present. Our aim is to connect these dependencies with the different formation paths of slow rotators and to disentangle nurture vs. nature in their formation.

EAGLE is an ideal testbed for our analysis, as it has been shown to reproduce the size-stellar mass relation (**?**Katsianis et al. 2017) and the specific angular momentum-stellar mass relation (Lagos et al. 2017; Swinbank et al. 2017) throughout time, both of which reflect the ability of the simulation to reproduce structural and dynamical properties of galaxies. In addition, EAGLE reproduces very well the evolution of SFR properties of galaxies (Furlong et al. 2015), colours (Trayford et al. 2015), the gas contents of galaxies (Bahé et al. 2016; Lagos et al. 2015, 2016; Crain et al. 2016), and produces both a blue cloud of predominantly disky galaxies, and a red sequence of mostly elliptical galaxies (Correa et al. 2017).

This paper is organised as follows. In § 2 we briefly describe the EAGLE simulation suite and introduce the IFU-like cubes and the kinematic properties we measure in the simulated galaxies. § 3 presents an analysis of the kinematic properties of simulated galaxies at $z = 0$ and the dependence on mass, environment and morphology. Here, we also present a thorough comparison with observations. In § 4 we study the physical origin of slow rotators in EAGLE by connecting kinematics with the formation history of galax-

Table 1. Features of the EAGLE Ref-L100N1504 and Ref-L050N752 and simulations used in this paper. The rows list: (1) initial particle masses of gas and (2) dark matter, (3) comoving Plummer-equivalent gravitational softening length, and (4) maximum physical gravitational softening length. Units are indicated in each row. EAGLE adopts (3) as the softening length at $z \geqslant 2.8$, and (4) at $z < 2.8$. These two simulations have volumes of side $L = 100$ and 50 cMpc^3, respectively.

	Property	Units	Value
(1)	gas particle mass	$[\mathrm{M}_\odot]$	1.81×10^6
(2)	DM particle mass	$[\mathrm{M}_\odot]$	9.7×10^6
(3)	Softening length	[ckpc]	2.66
(4)	max. gravitational softening	[pkpc]	0.7

ies. We present a discussion of our results and our main conclusions in § 5. Finally, Appendix A presents our convergence studies.

2 THE EAGLE SIMULATION

The EAGLE simulation suite (described in detail by Schaye et al. 2015, hereafter S15, and Crain et al. 2015, hereafter C15) consists of a large number of cosmological hydrodynamic simulations with different resolutions, cosmological volumes and subgrid models, adopting the Planck Collaboration (2014) cosmological parameters. S15 introduced a reference model, within which the parameters of the sub-grid models governing energy feedback from stars and accreting black holes (BHs) were calibrated to ensure a good match to the $z = 0.1$ galaxy stellar mass function and the sizes of present-day disk galaxies.

In Table 1 we summarise the parameters of the simulation used in this work, including the number of particles, volume, particle masses, and spatial resolution. Throughout the text we use pkpc to denote proper kiloparsecs and cMpc to denote comoving megaparsecs. A major aspect of the EAGLE project is the use of state-of-the-art sub-grid models that capture unresolved physics. The sub-grid physics modules adopted by EAGLE are: (i) radiative cooling and photoheating (Wiersma et al. 2009a), (ii) star formation (Schaye & Dalla Vecchia 2008), (iii) stellar evolution and chemical enrichment (Wiersma et al. 2009b), (iv) stellar feedback (Dalla Vecchia & Schaye 2012), and (v) black hole growth and active galactic nucleus (AGN) feedback (Rosas-Guevara et al. 2015). In addition, the fraction of atomic and molecular gas in a gas particle is calculated in post-processing following Rahmati et al. (2013) and Lagos et al. (2015).

The EAGLE simulations were performed using an extensively modified version of the parallel N-body smoothed particle hydrodynamics (SPH) code GADGET-3 (Springel 2005). Among those modifications are updates to the SPH technique and time stepping, which are collectively referred to as 'ANARCHY' (see Schaller et al. 2015 for an analysis of the impact of these changes on the properties of simulated galaxies compared to standard SPH). We use SUBFIND (Springel et al. 2001; Dolag et al. 2009) to identify self-bound overdensities of particles within halos (i.e. substructures). These substructures are the galaxies in EAGLE.

In addition to the EAGLE suite, we also analyse the HYDRANGEA suite presented in Bahé et al. (2017). This suite consists of 24 cosmological zoom-in simulations of galaxy clusters and their large scale environments in the halo mass range $M_{200} = 10^{14} - 10^{15.4}\,\mathrm{M}_\odot$, with M_{200} denoting the total mass within a sphere of radius r_{200}, within which the average density equals 200 times the critical density. These clusters were simulated with the same EAGLE reference model, but with a higher temperature to which AGN heat nearby gas particles, $\Delta T_{\rm AGN}$, and a higher viscosity parameter, $C_{\rm visc}$, that controls the effect of angular momentum on black hole gas accretion. The reference EAGLE model adopted $\Delta T_{\rm AGN} = 10^{8.5}$K and $C_{\rm visc} = 2\pi$, while HYDRANGEA adopted $\Delta T_{\rm AGN} = 10^{9}$K and $C_{\rm visc} = 2\pi \times 10^2$ (this model is referred to as AGNdT9 in S15; see their Table 3). **S15 compared the stellar mass function and size-mass relation at $z = 0$ of these two models (their Figs. 9 and 11), and showed that they agree to better than 10% and 20%, respectively.** The HYDRANGEA outputs were analysed with the same tools employed in EAGLE, and described above. In Appendix A2 we compare the AGNdT9 and reference models on the same box, number of particles and initial conditions, and show that AGNdT9 tends to produce a very similar number of slow rotators at $10^{9.5}\,\mathrm{M}_\odot \lesssim \mathrm{M}_{\rm stars} \lesssim 10^{11}\,\mathrm{M}_\odot$ compared to the reference EAGLE model ($\approx 9\%$).

Throughout the text we will refer to 'central' and 'satellite' galaxies, where the central corresponds to the galaxy hosted by the main subhalo of a Friends-of-Friends halo, while other subhalos within the group host satellite galaxies (Qu et al. 2017). Lagos et al. (2017) showed in a study of the specific angular momentum evolution of galaxies in EAGLE, that an appropriate stellar mass cut above which galaxies have angular momentum profiles converged is $M_{\rm stars} > 5 \times 10^9\,\mathrm{M}_\odot$. Thus, we adopt that threshold in this work (see Appendix A1 for a convergence study). EAGLE **and** HYDRANGEA **have $5,587$ and $10,771$ galaxies, respectively, at $z = 0$ above this mass threshold and this is the sample we use in this work.**

2.1 Kinematic measurements

In this paper we measure the r-band luminosity-weighted line-of-sight velocity, velocity dispersion, stellar spin parameter $\lambda_{\rm R}$, and ellipticity of all galaxies in EAGLE in the simulations presented in Table 1 and the HYDRANGEA clusters. We describe our procedure below.

We first construct the stellar kinematic maps for each galaxy by projecting them onto a 2-dimensional plane. We use two orientations: an edge-on view, in which the stellar spin is oriented along the y-axis of the image, and a random view, in which the line-of-sight is along the z-axis of the simulated box. We bin this 2-dimensional image onto pixels of width w and construct a r-band luminosity-weighted velocity distribution for each bin, using the centre of potential of the galaxy as the rest frame. We adopted $w = 1.5\,\mathrm{pkpc}$ (approximately twice the softening length of EAGLE; see Table 1). In Appendix A3 we show that the kinematic properties we are measuring here are converged to better than 10%. We only see significant convergence issues if the bin is chosen to be close to the softening length of the simulation **or in galaxies of stellar masses $\approx 5 \times 10^9\,\mathrm{M}_\odot$ when the bin is too similar to their** r_{50}. The chosen bin of 1.5 pkpc is very similar to the average spatial resolution of SAMI galaxies (1.6 pkpc; van de Sande et al. 2017).

We fit a Gaussian to the r-band luminosity line-of-sight velocity distribution of each pixel, and define the rotational velocity as the velocity at which the Gaussian peaks, and the velocity dispersion as the square root of the variance. This procedure closely mimics the measurements performed in integral field spectroscopic (IFS) surveys, such as ATLAS^{3D} (Cappellari et al. 2011) and SAMI (van de Sande et al. 2017). The result of this proce-

dure is shown in Fig. 1 for 4 relatively massive galaxies in the Ref-L050N752 simulation, 2 star-forming and 2 passive, oriented edge-on. For this visualization we use the KINEMETRY package of Krajnović et al. (2006), and for the colour scale of the rotational velocity maps we adopt the range $[-V_{\rm max}, V_{\rm max}]$. Here, $V_{\rm max}$ is the maximum circular velocity expected for the stellar mass of the galaxy assuming the Tully-Fisher relation measured by Dutton et al. (2011). The purpose of this colour scheme is to make slow rotation visually evident. In general, we find that at fixed stellar mass, passive galaxies tend to be rounder and more slowly rotating than star-forming galaxies. We will come back to this in § 3.

We construct velocity and luminosity maps, such as those in Fig. 1, for all galaxies in the simulations of Table 1 and in the HYDRANGEA cluster suite at $z = 0$. From these maps we calculate the r-band luminosity-weighted spin parameter, $\lambda_{\rm R}$ and ellipticities, ϵ, at radii $0.5, 1, 1.5, 2, \times {\rm r}_{50}$, with r_{50} being the projected half-stellar mass radius. We first calculate ϵ as in Cappellari et al. (2007),

$$\epsilon = 1 - \sqrt{\frac{a^2}{b^2}}, \tag{1}$$

where,

$$\begin{aligned} a^2 &= \frac{\bar{x}^2 + \bar{y}^2}{2} + \sqrt{\left(\frac{\bar{x}^2 - \bar{y}^2}{2}\right)^2 + \bar{xy}}, \\ b^2 &= \frac{\bar{x}^2 + \bar{y}^2}{2} - \sqrt{\left(\frac{\bar{x}^2 - \bar{y}^2}{2}\right)^2 + \bar{xy}}, \end{aligned} \tag{2}$$

and,

$$\bar{x}^2 = \frac{\sum_i L_i\, x_i^2}{\sum_i L_i},\ \bar{y}^2 = \frac{\sum_i L_i\, y_i^2}{\sum_i L_i},\ \bar{xy} = \frac{\sum_i L_i\, x_i\, y_i}{\sum_i L_i}. \tag{3}$$

Here, i corresponds to the pixels inside the aperture in which we wish to measure ϵ, L_i is the r-band luminosity contained in the pixel, (x_i, y_i) are the x and y positions of the selected pixels. This measurement of ϵ is equivalent to diagonalizing the inertia tensor of the galaxy's stellar surface density. We also calculate the position angle of the major axis of the galaxy (measured counter clockwise from $y = 0$) as

$$\theta_{\rm PA} = {\rm atan}\left(\frac{2\,\bar{xy}}{\bar{x}^2 - \bar{y}^2}\right). \tag{4}$$

We calculate ϵ within circular apertures of radii $0.5, 1, 1.5, 2 \times$ r$_{50}$. Examples of the values of ϵ obtained via this method are shown in Fig. 1. We then calculate $\lambda_{\rm R}$ as

$$\lambda_{\rm R} = \frac{\sum_i L_i\, r_i |V_i|}{\sum_i L_i\, r_i \sqrt{V_i^2 + \sigma_i^2}}, \tag{5}$$

where V_i and σ_i are the r-band luminosity-weighted line-of-sight mean and standard deviation velocities in the pixel i calculated as described above, and r_i is the distance from the centre of the galaxy to the pixel (i.e. the circular radius). As in Emsellem et al. (2011), to measure these quantities within r, we include only pixels enclosed by the ellipse of major axis r, ellipticity $\epsilon(r)$ and position angle $\theta_{\rm PA}$(r).

IFS surveys typically compare ϵ and $\lambda_{\rm R}$ measured within the same aperture (typically an effective radius; e.g. Emsellem et al. 2011 and van de Sande et al. 2017). We follow this and compare $\lambda_{\rm R}$ and ϵ measured within r_{50}, and refer to these as $\lambda_{r_{50}}$ and $\epsilon_{r_{50}}$, respectively, unless otherwise stated.

2.2 Galaxy mergers

We use the merger trees available in the EAGLE database (McAlpine et al. 2015) to identify galaxy mergers. These merger trees were created using the D − Trees algorithm of Jiang et al. (2014). Qu et al. (2017) described how this algorithm was adapted to work with EAGLE outputs. Galaxies that went through mergers have more than one progenitor, and for our purpose, we track the most massive progenitors of merged galaxies, and compare the kinematic properties of those with that of the merger remnant. The trees stored in the public database of EAGLE connect 29 epochs. The time span between snapshots can range from $\approx$ 0.3 Gyr to $\approx$ 1 Gyr. Lagos et al. (2018) showed that these timescales are appropriate to study the effect of galaxy mergers on the specific angular momentum of galaxies, as mergers roughly take that time to settle.

We split mergers into major and minor mergers. The former are those with a stellar mass ratio between the secondary and the primary galaxy $\geqslant 0.3$, while minor mergers have a mass ratio between 0.1 and 0.3. Lower mass ratios are classified as smooth accretion (Crain et al. 2016). In addition, and following Lagos et al. (2018), we split mergers into gas-rich (wet) and gas-poor (dry) based on the neutral gas (atomic plus molecular) to stellar mass ratio of the merger:

$$R_{\rm gas,merger} \equiv \frac{M^{\rm s}_{\rm neutral} + M^{\rm p}_{\rm neutral}}{M^{\rm s}_{\rm stars} + M^{\rm p}_{\rm stars}}, \tag{6}$$

where $M^{\rm s}_{\rm neutral}$ and $M^{\rm p}_{\rm neutral}$ are the neutral gas masses of the secondary and primary galaxies, respectively, while $M^{\rm s}_{\rm stars}$ and $M^{\rm p}_{\rm stars}$ are the corresponding stellar masses. Here we classify mergers with $R_{\rm gas,mergers} \leqslant 0.1$ as dry, and the complement as wet. For dry mergers, the average $R_{\rm gas,merger}$ is ≈ 0.02.

We calculate the orbital specific angular momentum of the merger, $j_{\rm orbital}$, as $j_{\rm orbital} = |\vec{r} \times \vec{v}|$, with $\vec{r}$ and $\vec{v}$ being the position and velocity vectors, respectively, of the secondary galaxy in the rest frame of the primary.

Masses are measured within an aperture of 30 pkpc. Neutral gas fractions of individual particles in EAGLE are calculated as in Rahmati et al. (2013) and Lagos et al. (2015).

3 KINEMATIC PROPERTIES OF EAGLE GALAXIES

We visually inspect the kinematic morphology of galaxies in the $\lambda_{r_{50}}$-ϵ plane, which has been proposed by Emsellem et al. (2007) as an effective way of distinguishing slow and fast rotators. Fig. 2 shows the rotational velocity maps of randomly selected galaxies in bins of $\lambda_{r_{50}}$ and ϵ. We construct the maps as in Fig. 1. Lines indicate different ways of defining slow rotators from the literature. There is an evident transition at around $\lambda_{r_{50}} \approx 0.2$ below which galaxies **appear** deficient in rotation. **By inspecting the edge-on oriented velocity maps of galaxies that are classified as slow rotators in EAGLE, we confirm their deficient rotation out to $3\,r_{50}$.** If EAGLE galaxies are a good representation of real ones, this would mean that slow rotators would be classified as such even if we had kinematics extending out to much larger radii than available (typically kinematics is available only at $r < r_{50}$). On the other hand,

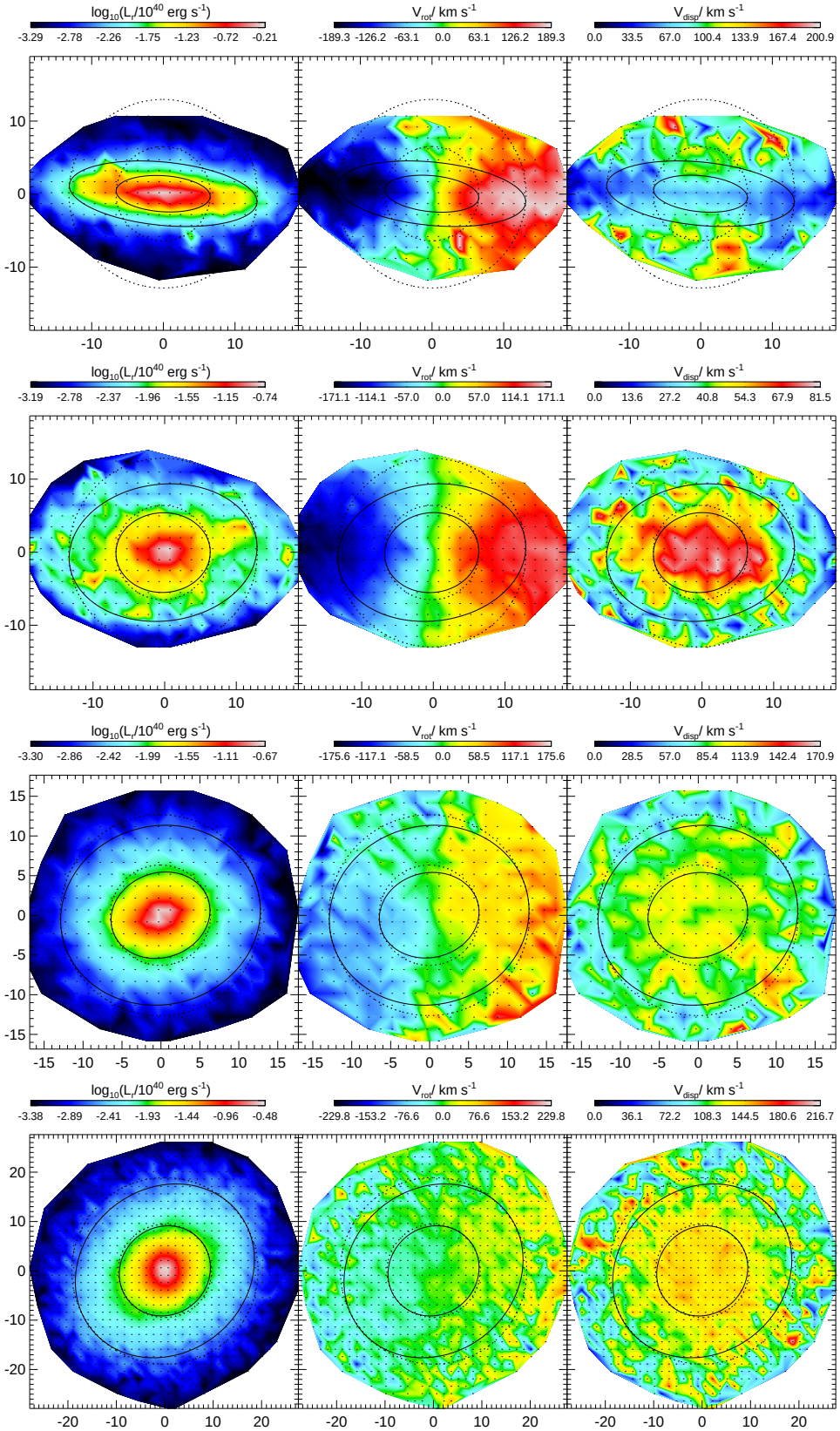

Figure 1. Examples of an edge-on view of the r-band luminosity (left), rotation (middle) and velocity dispersion (right) fields of 4 galaxies with $2 \times 10^{10}\,\mathrm{M}_\odot < \mathrm{M}_{\mathrm{stars}} < 4 \times 10^{10}\,\mathrm{M}_\odot$ at $z = 0$ in the Ref-L050N752 simulation. Axes show distance from galaxy centre in pkpc. The top 2 galaxies have $\mathrm{SFR} > 1\,\mathrm{M}_\odot\,\mathrm{yr}^{-1}$, while the bottom 2 have $\mathrm{SFR} < 0.2\,\mathrm{M}_\odot\,\mathrm{yr}^{-1}$. The colour scales are indicated at the top of each panel, and in the case of the rotational velocity map, we force the range $[-V_{\mathrm{max}}, V_{\mathrm{max}}]$, where V_{max} is the maximum circular velocity expected for the stellar mass of the galaxy given the Tully-Fisher relation measured by Dutton et al. (2011). The physical scale of the images is shown along the axes and is in pkpc. Circles show 1 and $2\,r_{50}$ of the galaxies, while ellipses are constructed using our ellipticity measurements at 1 and $2\,r_{50}$ (see Eq. 1). From top to bottom, the values of $\epsilon_{r_{50}}$ are 0.65, 0.6, 0.12 and 0.07, respectively.

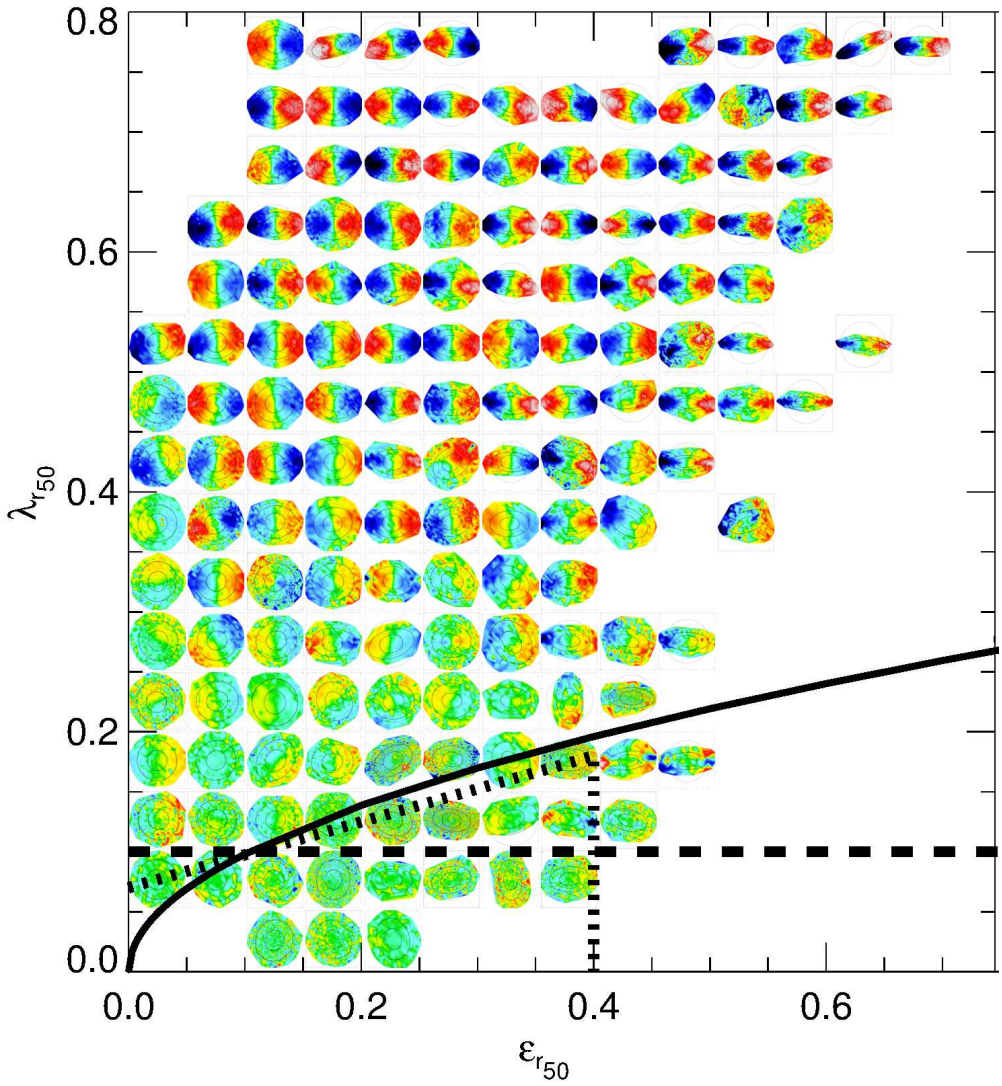

Figure 2. Rotational velocity field of randomly selected galaxies in the $\lambda_{r_{50}}$-$\epsilon_{r_{50}}$ plane from the Ref-L050N752 simulation. Galaxies here are randomly oriented. The colour scales of the maps and circles/ellipses are as in Fig. 1. Lines show the classification of slow rotators from Emsellem et al. (2007), Emsellem et al. (2011) and Cappellari (2016), as dashed, solid and dotted lines, respectively.

galaxies with $0.2 \lesssim \lambda_{r_{50}} \lesssim 0.4$ reach their expected rotational velocity at $2-3\,r_{50}$, while galaxies with $\lambda_{r_{50}} \gtrsim 0.4$ reach it by $\approx r_{50}$. Fig. 2 indicates that $\lambda_{r_{50}}$ is a good proxy for the kinematic structure of galaxies, as suggested by Emsellem et al. (2007, 2011).

In Fig. 3 we visually compare the positions of galaxies in the $\lambda_{r_{50}}$-ϵ plane in the Ref-L100N1504 and HYDRANGEA simulations with those of the observational surveys ATLAS^{3D} (Emsellem et al. 2011), MASSIVE (Veale et al. 2017a) and SAMI (van de Sande et al. 2017). The former two are volume-limited surveys of early-type galaxies, while SAMI is a stellar mass selected survey, thus including both late and early types. Since we include all galaxies with $M_{\rm stars} > 5\times10^9\,{\rm M}_\odot$ in the simulations, our results may be more comparable to SAMI. The sizes and colours of the symbols scale with stellar mass, so that the most massive galaxies appear as larger symbols.

SAMI appears to have systematically lower $\lambda_{r_{50}}$ compared to ATLAS^{3D}, which is not surprising as the measurements are not performed exactly in the same way. In ATLAS^{3D}, Emsellem et al. (2011) adopted the radial distance to the luminosity centre as r_i in Eq. 5, while in SAMI, van de Sande et al. (2017) adopted the semi major axis of the ellipse that goes through the given bin as r_i in Eq. 5.

Our calculation of $\lambda_{r_{50}}$ resembles more closely that in ATLAS^{3D}. In the three surveys, galaxies with $M_{\rm stars} \gtrsim 10^{11.5}\,{\rm M}_\odot$ (largest symbols in Fig. 3) preferentially have low $\lambda_{r_{50}}$, and the same is seen to some extent in the HYDRANGEA simulation, but in the Ref-L100N1504 simulation all massive galaxies are slightly above the observational delimitation of slow rotators. Compared to MASSIVE (middle panel in Fig. 3), it is apparent that our simulations do not produce the right fraction of slow rotators at the very massive end. We will come back to this in § 3.1.

Both simulations lack the very high ellipticity galaxies, $\epsilon_{r_{50}} \gtrsim 0.7$. The latter may be due to the subgrid interstellar medium physics included in the simulations, which prevents very flat Milky-Way like disks from forming. In EAGLE a global temperature floor, $T_{\rm eos}(\rho)$, is imposed corresponding to a polytropic equation of state

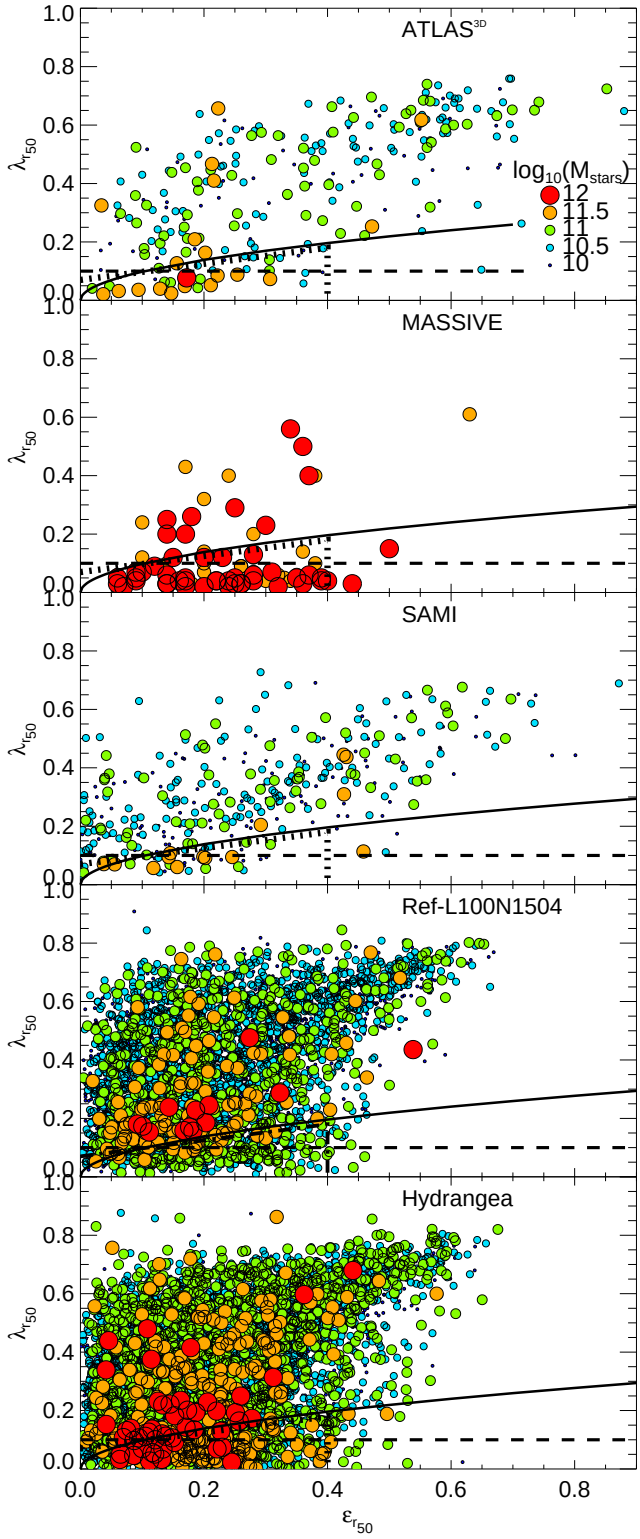

Figure 3. $\lambda_{r_{50}}$ as a function of $\epsilon_{r_{50}}$ for galaxies in the ATLAS^{3D} (Emsellem et al. 2011; top panel), MASSIVE (Veale et al. 2017a; second panel) and SAMI (van de Sande et al. 2017; third panel) surveys, and for the simulations Ref-L100N1504 (fourth panel) and HYDRANGEA (bottom panel). Galaxies in the two simulations are randomly oriented. Lines show the classification of slow and fast rotators from Emsellem et al. (2007), Emsellem et al. (2011) and Cappellari (2016), as dashed, solid and dotted lines, respectively. Sizes and colours of the symbols correspond to different stellar masses, as labelled in the top panel.

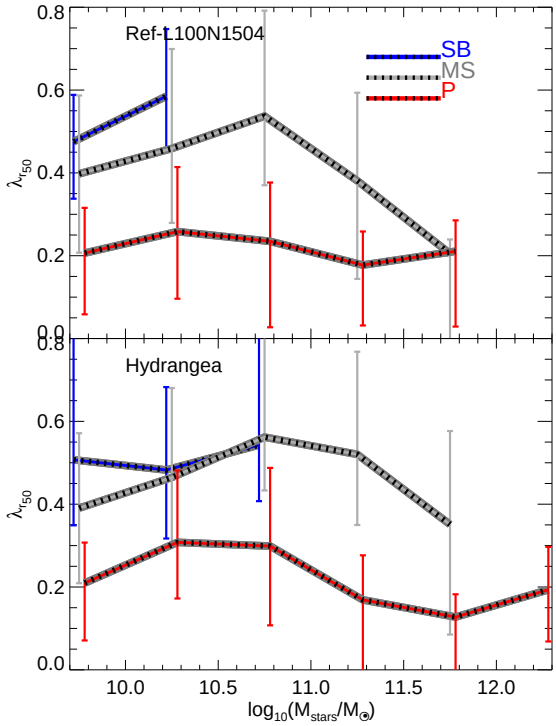

Figure 4. $\lambda_{r_{50}}$ as a function of stellar mass for galaxies in the Ref-L100N1504 (top panel) and HYDRANGEA (bottom panel) simulations. Lines and error bars show the median and $16^{\rm th}-84^{\rm th}$ percentile ranges, respectively, for galaxies that are classifies as starburst (SB), main sequence (MS) or passive (P), as labelled. We define the above samples based on δ MS: > 4, $0.1 - 4$, < 0.1. Only bins with $\geqslant 5$ objects are shown.

$P_{\rm eos} \propto \rho^{\gamma_{\rm eos}}$, normalized to $T_{\rm eos} = 8,000$ K and $n_{\rm H} = 0.1\,{\rm cm}^{-3}$. In addition, a second temperature floor of $8,000$ K is imposed on gas with $n_{\rm H} > 10^{-5}\,{\rm cm}^{-3}$, preventing the metal-rich gas from cooling below that threshold. This sets a minimum disk height of $\lesssim 1$ kpc, larger than the Milky-Way or other grand-design spiral galaxies, which exhibit scaleheights typically of ≈ 0.4 kpc (Kregel et al. 2002). Thus, it is not surprising that very flat galaxies do not exist in EAGLE or HYDRANGEA. Appendix A1 shows that increasing the resolution by a factor of 8 in mass and 2 in spatial resolution does not significantly change the ellipticity of galaxies, supporting our conclusion. **The topic of convergence in the formation of elliptical galaxies is contingent. Bois et al. (2010) performed a resolution study of idealised galaxy mergers and concluded that the product of wet mergers was resolution dependant, and that their role on the formation of slow rotators may be underestimated in simulations such as EAGLE. However, more recently Sparre & Springel (2016, 2017) showed in cosmological zooms of galaxy mergers that environment and feedback play a decisive role in the fate of the remnant, more so than the resolution. Our resolution tests show no evidence for convergence issues at the stellar masses we are investigating, on average, but we cannot rule out that individual cases may be more affected.**

Fig. 4 shows $\lambda_{r_{50}}$ as a function of stellar mass for galaxies in the Ref-L100N1504 and HYDRANGEA simulations at $z = 0$. We use different symbols to show starburst, main sequence and passive galaxies. We define the latter in terms of their specific star formation rate, ${\rm sSFR} = {\rm SFR}/{\rm M_{stars}}$, relative to the main sequence at

that stellar mass. We calculate the latter as in Furlong et al. (2015). In short, the main sequence is calculated as the median sSFR of all galaxies that have sSFR$> 0.01\,\mathrm{Gyr}^{-1}$ in a bin of stellar mass. We refer to the this as $\langle sSFR(M)\rangle$. We then calculate the sSFR of galaxies relative to the main sequence,

$$\delta\,\mathrm{MS} = \frac{\mathrm{sSFR}}{\langle \mathrm{sSFR(M)}\rangle}. \quad (7)$$

Starburst (SB), main sequence (MS) and passive galaxies are classified as those with $\delta\,\mathrm{MS} \geqslant 4$, $0.1 < \delta\,\mathrm{MS} < 4$ and $\delta\,\mathrm{MS} < 0.1$, respectively.

In both simulations passive galaxies tend to have a lower $\lambda_{r_{50}}$ than MS galaxies at fixed stellar mass. SB galaxies have a slightly higher median $\lambda_{r_{50}}$ than MS galaxies but the scatter is much larger. In HYDRANGEA most of the galaxies with $M_{\rm stars} \gtrsim 10^{11.7}\,\mathrm{M}_\odot$ are passive, which is expected given that the environments of these simulations are designed to represent the densest in the Universe. We also see that MS galaxies show a clear peak at $M_{\rm stars} \approx 10^{10.8}\,\mathrm{M}_\odot$ below and above which galaxies display a decrease in $\lambda_{r_{50}}$. This peak is also seen in the FIRE simulations (El-Badry et al. 2018). Passive galaxies also exhibit a peak but only in the HYDRANGEA simulation, which may be due to poor statistics in the passive population in the Ref-L100N1504 simulation below that transition mass.

3.1 The fraction of slow rotators in EAGLE

Due to the availability of large IFS surveys, there has been a lot of recent interest in how the fraction of slow rotators depends on stellar mass and environment. Veale et al. (2017b), Brough et al. (2017) and Greene et al. (2017) found that the fraction of slow rotators depends strongly on stellar mass, with a very weak dependence on environment once stellar mass is controlled for. Similar results have been reported from the study of galaxy shapes (Pasquali et al. 2007). The complementarity of EAGLE and HYDRANGEA in dynamical mass allows us to explore a very wide range of environments and hence to study this question.

Fig. 5 shows the fraction of slow rotators, $\mathrm{F_{SR}}$, as a function of stellar mass at $z = 0$ in the Ref-L100N1504 and HYDRANGEA simulations, using the 3 definitions of slow rotators shown in Fig. 3. The two simulations agree well at $M_{\rm stars} \lesssim 10^{10.8}\,\mathrm{M}_\odot$ within the uncertainties, but there are some differences worth noting. Both simulations show that there is a clear transition at $M_{\rm stars} \approx 10^{11}\,\mathrm{M}_\odot$ above which $\mathrm{F_{SR}}$ starts to raise quickly, except for the highest mass bin, in which we see a downturn. In the case of the Ref-L100N1504 simulation, this is due to applying the observational classification of slow rotators without considering any errors. A small **Gaussian error of width** 0.05 in $\lambda_{\rm R}$ leads to a monotonically rising $\mathrm{F_{SR}}$ (dotted lines in Fig. 5). HYDRANGEA displays a downturn at much larger masses ($> 10^{11.5}\,\mathrm{M}_\odot$), and we show in Fig. 7 that this is due to the properties of the brightest cluster galaxies (BCGs) in HYDRANGEA. BCGs here are defined as the central galaxy of halos with masses $> 10^{14}\,\mathrm{M}_\odot$. Because the HYDRANGEA suite covers large regions around the 24 resimulated clusters (out to $10\,\mathrm{r_{200}}$), there are in total 34 halos with those masses in the suite, and thus the same number of BCGs.

In Fig. 5 we also show a compilation of observations from the SAMI, ATLAS^{3D} and MASSIVE surveys. Both simulations agree remarkably well with the observations at $M_{\rm stars} \lesssim 10^{11.2}\,\mathrm{M}_\odot$, with some tension arising at $M_{\rm stars} \gtrsim 10^{11.5}\,\mathrm{M}_\odot$. We show below that this is caused by unrealistic properties of our simulated

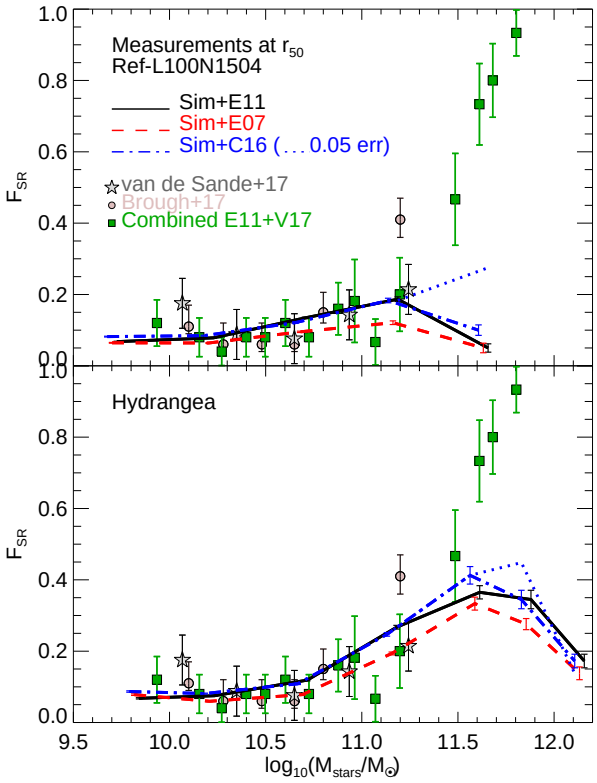

Figure 5. The fraction of slow rotators, $\mathrm{F_{SR}}$ as a function of stellar mass in the Ref-L100N1504 (top panel) and HYDRANGEA (bottom panel) simulations. We classified slow rotators using the Emsellem et al. (2007) (red dashed line), Emsellem et al. (2011) (black solid line) and Cappellari (2016) (blue dot-dashed line) criteria. We also show the observations from the SAMI (van de Sande et al. 2017), the SAMI-clusters (Brough et al. 2017), MASSIVE (Veale et al. 2017a) and ATLAS^{3D} (Emsellem et al. 2011) surveys. The latter two are presented in combination (combined E11+V17) . Error bars show 1 standard deviation calculated with 10 jackknife resamplings in each stellar mass bin. Dotted lines show $\mathrm{F_{SR}}$ adopting the Cappellari (2016) criterion **after applying a Gaussian error of width** 0.05 **to the values of** $\lambda_{\rm R}$.

BCGs. In our simulations, $\mathrm{F_{SR}}$ does not rise above ≈ 0.7 in disagreement with the observations. We show later (Fig. 7) that $\mathrm{F_{SR}}$ at $M_{\rm stars} \gtrsim 10^{11.2}\,\mathrm{M}_\odot$ is very sensitive to environmental effects and a slightly different preference for satellites over central galaxies can significantly skew $\mathrm{F_{SR}}$.

The effect of satellite/central galaxies in the Ref-L100N1504 and HYDRANGEA simulations is shown in Fig. 6. For clarity, we only show the classifications of slow rotators of Cappellari (2016). Adopting instead the Emsellem et al. (2007, 2011) classifications does not alter the conclusions. Both simulations show satellite galaxies having a larger $\mathrm{F_{SR}}$ compared to centrals (red vs. blue lines), **particularly visible at** $M_{\rm stars} \gtrsim 10^{10.8}\,\mathrm{M}_\odot$. However, when selecting only passive galaxies (Fig. 7), centrals have a much larger $\mathrm{F_{SR}}$ compared to satellites at $M_{\rm stars} \lesssim 10^{11}\,\mathrm{M}_\odot$. This is expected as the quenching of central galaxies is typically accompanied by morphological transformation, while for satellite galaxies this is not necessary as they quench due to the environment they live in (e.g. Trayford et al. 2016; Dubois et al. 2016). The differences between satellites and centrals at fixed stellar mass are significant. We performed Kolmogorov-Smirnov tests in narrow bins of stellar

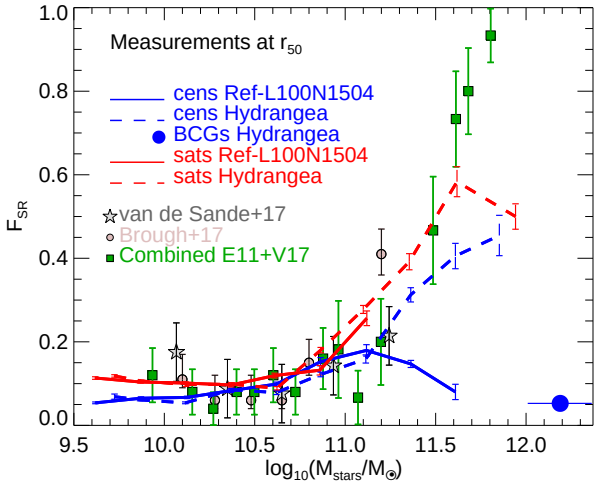

Figure 6. $\mathrm{F_{SR}}$, as defined by the Cappellari (2016) classification, as a function of stellar mass, for galaxies at $z = 0$ in the Ref-L100N1504 (solid lines) and HYDRANGEA (dashed lines) simulations. Central and satellite galaxies are shown in blue and red, as labelled. For the HYDRANGEA simulation we show separately $F_{\rm SR}$ for the brightest cluster galaxies as a solid symbol. The horizontal error bar in the latter shows the $25^{\rm th} - 75^{\rm th}$ percentile range.

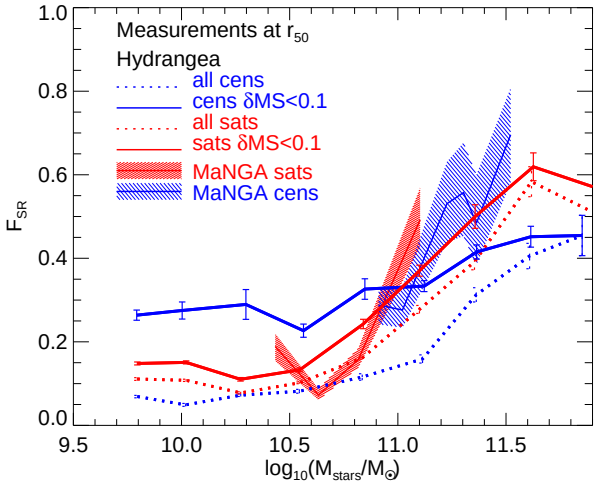

Figure 7. The fraction of slow rotators obtained by applying the Cappellari (2016) classification to the HYDRANGEA simulations, separating central and satellite galaxies. BCGs are not included in this figure. Dotted lines show all galaxies in the samples, while solid lines show the subsample of galaxies that have a SSFR relative to the MS $\leqslant 0.1$. The observations of Greene et al. (2017) using MaNGA early-type galaxies are shown as lines with shaded regions indicating the 1σ scatter.

mass to quantify how different the $\lambda_{\rm r_{50}}$ distributions between these two populations are and found typical p values < 0.05.

Central galaxies in the HYDRANGEA simulation show a decrease in $F_{\rm SR}$ in the highest mass bin. This decrease is significant and is driven by the contribution of BCGs (central galaxies of halos with masses $\geqslant 10^{14}\,\mathrm{M}_\odot$). To make this clearer, we show separately $F_{\rm SR}$ for BCGs in HYDRANGEA as a filled symbol. Recently, Oliva-Altamirano et al. (2017) analysed a sample of local Universe BCGs and found a large fraction of slow rotators, $\approx 50\%$, significantly larger than what we obtain in HYDRANGEA. Bahé et al. (2017) showed that BCGs in HYDRANGEA are too massive for their halo mass and have some remaining star formation that is higher than in observations. Several simulations have shown that continuing star formation can efficiently spin galaxies up (Moster et al. 2011; Naab et al. 2014; Lagos et al. 2017; Penoyre et al. 2017), and thus it is not surprising that in HYDRANGEA BCGs are mostly fast rotators. It is therefore likely that more efficient feedback at high redshift would not only lead to more realistic stellar masses and star formation rates of these BCGs, but also increase their slow rotator fraction (see also Barnes et al. 2017).

Fig. 7 also shows that satellite galaxies reach an $\mathrm{F_{SR}} \gtrsim 0.5$ at $M_{\rm stars} \approx 10^{11.5}\,\mathrm{M}_\odot$ in better agreement with the observations. Since both surveys, ATLAS$^{\rm 3D}$ and MASSIVE, are volume-limited, $\approx 42\%$ of those are satellite galaxies, 24% are brightest group/cluster galaxies, and the rest are field galaxies. Thus, it is not surprising that satellite galaxies better follow the results from MASSIVE. In the Ref-L100N1504 and HYDRANGEA simulations there is a clear environmental effect that becomes apparent when comparing satellites and centrals at fixed stellar mass (Fig. 6).

Recently Greene et al. (2017) found differences between satellite/central early-type galaxies in MaNGA of a similar magnitude to the one found in our simulations. Their observations are shown as shaded bands in Fig. 7. Greene et al. found that satellites are $\approx$ 20% more likely to be slow rotators than centrals. They, however, cautioned that due to the different spatial coverage and slightly different stellar mass distribution, this difference between satellites and centrals is not obviously significant. In EAGLE and HYDRANGEA, the $\mathrm{F_{SR}}$ differences between these two populations are present over the entire mass range, albeit with differences been very small at $M_{\rm stars} < 10^{10.5}\,\mathrm{M}_\odot$. Note, however, that the Greene et al. (2017) slow rotator fraction is generally higher than both the Ref-L100N1504 and HYDRANGEA simulations and the observations from ATLAS$^{\rm 3D}$, SAMI and MASSIVE.

Greene et al. (2017) measured $\lambda_{\rm R}$ out to larger radii than ATLAS$^{\rm 3D}$, SAMI and MASSIVE, and in addition they measured ellipticities from a single Sèrsic index fit to their images. Greene et al. (2017) adapted the slow rotator classification criteria of Emsellem et al. (2011) to work with their measurements, and argued that about 10% of their galaxies would change classification from slow to fast rotators if the measurements were done at r_{50}. Nonetheless, the reported $F_{\rm SR}$ is higher by a factor of $\approx 25\%$ at least compared to other IFS surveys; hence, there probably are other systematic effects that have not yet been taken into account. Since these authors analysed only early-type galaxies, we also show in Fig. 7 the $\mathrm{F_{SR}} - \mathrm{M_{stars}}$ relation for passive galaxies (those with a $\delta\,\mathrm{MS} < 0.1$). $F_{\rm SR}$ is higher for this subsample but not enough as to agree with Greene et al. (2017). Interestingly, in this subsample we find the $F_{\rm SR}$ of centrals being $2/3$ times larger than for satellites **at** $M_{\rm stars} \lesssim 10^{10.7}\,\mathrm{M}_\odot$.

We explore the effect of environment on $\mathrm{F_{SR}}$ further by studying the dependence on halo mass for centrals and satellite galaxies in Fig. 8. Here, we combined the galaxy populations of the Ref-L100N1504 and HYDRANGEA simulations at $z = 0$. The top panel of Fig. 8 shows central galaxies. There is a trend of increasing $\mathrm{F_{SR}}$ with increasing halo mass, at fixed stellar mass. Since stellar and halo mass are well correlated for central galaxies in EAGLE (Schaye et al. 2015; Guo et al. 2015), the overlap in stellar mass between the different halo mass bins is only partial. We quantify the

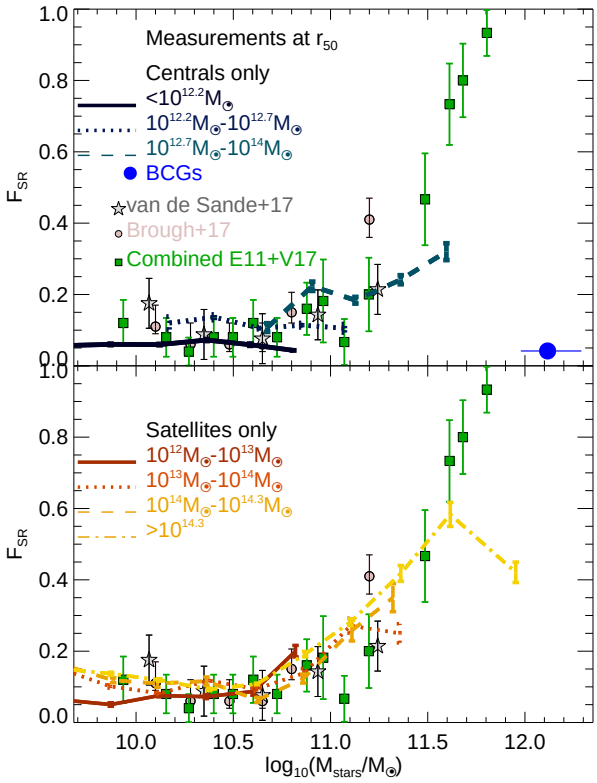

Figure 8. *Top panel:* $F_{\rm SR}$ as a function of stellar mass for central galaxies at $z = 0$ in the combined galaxy sample of the Ref-L100N1504 and HYDRANGEA simulations. Here we only show the slow rotator classification of Cappellari (2016). Central galaxies are shown in 4 bins of halo mass: $< 10^{12.2}\,{\rm M}_\odot$ (solid line), $10^{12.2}\,{\rm M}_\odot - 10^{12.8}\,{\rm M}_\odot$ (dotted line), $10^{12.8}\,{\rm M}_\odot - 10^{14}\,{\rm M}_\odot$ (dashed line) and $> 10^{14}\,{\rm M}_\odot$ (filled circle; as in Fig. 7). Error bars show 1 standard deviation calculated with 10 jackknife resamplings in each stellar mass bin. Observations are shown as symbols, as labelled. *Bottom panel:* as in the top panel but for satellite galaxies. Here we adopt halo mass bins of: $10^{12}\,{\rm M}_\odot - 10^{13}\,{\rm M}_\odot$ (solid line), $10^{13}\,{\rm M}_\odot - 10^{14}\,{\rm M}_\odot$ (dotted line), $10^{14}\,{\rm M}_\odot - 10^{14.3}\,{\rm M}_\odot$ (dashed line) and $> 10^{14.3}\,{\rm M}_\odot$ (dot-dashed line). There is a weak but significant systematic effect of $F_{\rm SR}$ increasing with increasing halo mass at fixed stellar mass for central galaxies, with no clear trend in the case of satellites.

environmental dependence in the stellar mass range where overlap occurs: (i) at $M_{\rm stars} = 10^{10.1} - 10^{10.8}\,{\rm M}_\odot$, centrals hosted by halos of masses $10^{12.2}\,{\rm M}_\odot - 10^{12.7}\,{\rm M}_\odot$ are 2 times more likely to be slow rotators than centrals in halos of masses $< 10^{12.2}\,{\rm M}_\odot$; (ii) at $M_{\rm stars} = 10^{10.8} - 10^{11.1}\,{\rm M}_\odot$ centrals hosted by halos of masses $10^{12.7}\,{\rm M}_\odot - 10^{14}\,{\rm M}_\odot$ are $\approx 35\%$ more likely to be slow rotators than galaxies hosted by halos of masses $10^{12.2}\,{\rm M}_\odot - 10^{12.7}\,{\rm M}_\odot$. In Fig. 8 we show BCGs separately because their properties (i.e. overly massive and star-forming) lead to most of them being fast rotators.

In the bottom panel of Fig. 8 we show the effect of halo mass on the population of satellite galaxies. We see no evident effect of environment. However, when studying the subsample of passive satellite galaxies (i.e. those with $\delta\,{\rm MS} < 0.1$; see Eq. 7 for a definition) we see a strong environmental effect. This is shown in Fig. 9. We find that among passive satellites, $F_{\rm SR}$ *increases with decreasing halo mass* at $M_{\rm stars} \lesssim 10^{11}\,{\rm M}_\odot$. **The latter is clearly visible when we compare satellites in halos of masses below and above**

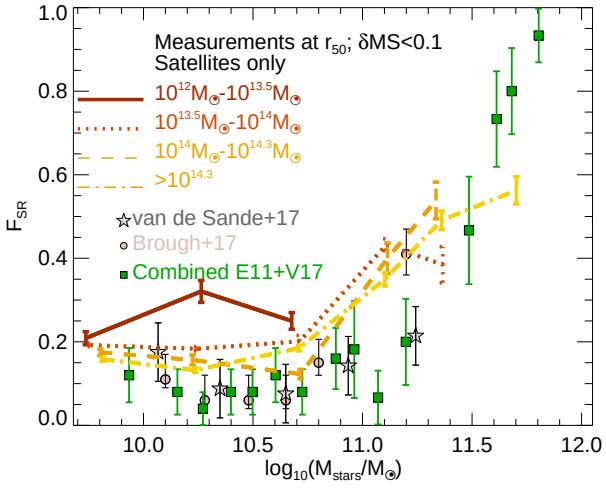

Figure 9. As in the bottom panel of Fig 8 but for passive satellites (i.e. those with $\delta\,{\rm MS} < 0.1$).

$10^{13}\,{\rm M}_\odot$. At higher masses the statistics are too poor to draw any conclusion. At first glance this result is unexpected, as the overall trend of satellites plus centrals shows more slow rotators in denser environments. We interpret this trend as due to passive satellites in low density environments being quenched at the same time as they go through a morphological transformation (Trayford et al. 2015; Dubois et al. 2016). The satellite population we are studying here are relatively massive galaxies, $M_{\rm stars} > 10^{10}\,{\rm M}_\odot$, which are unlikely to be quenched solely by environment in halos of masses $< 10^{13}\,{\rm M}_\odot$. In more massive halos, $M_{\rm halo} \gtrsim 10^{14}\,{\rm M}_\odot$, galaxies can quench without morphological transformation, through e.g. ram pressure and/or tidal stripping. Thus, our simulations prediction that a trend with halo mass should be seen for satellite galaxies, but only in the subsample of passive satellites. Selecting passive centrals increases the overall $F_{\rm SR}$, but does not significantly change the halo mass effect we described above (not shown here).

Veale et al. (2017b) and Brough et al. (2017) recently concluded that the dependence of $F_{\rm SR}$ on environment is fully accounted for by the stellar mass of galaxies: more massive galaxies live in denser environments, and thus no environmental effects are seen at fixed stellar mass. Brough et al. (2017) focused exclusively on cluster environments, and thus their galaxy population was vastly dominated by satellite galaxies. As we showed here, EAGLE and HYDRANGEA show that environmental effects (as manifested through a halo mass dependence) in the satellite galaxy population are minimal, and even less obvious in the cluster population alone (see dashed and dot-dashed lines in the bottom panel of Fig. 8). On the other hand, we predict that the halo mass effect on slow rotators should be detectable in the population of centrals and passive satellite galaxies, but only if a wide range of halo masses is explored, $10^{11}\,{\rm M}_\odot) \lesssim {\rm M}_{\rm halo} \lesssim 10^{15}\,{\rm M}_\odot$.

4 THE PHYSICAL ORIGIN OF SLOW ROTATORS

In this section we analyse the physical origin of slow rotators in two ways. First, we analyse the merger history of galaxies that at $z = 0$ are slow rotators to establish how correlated their low $\lambda_{\rm R}$ is with the presence and type of mergers they suffered throughout their lives,

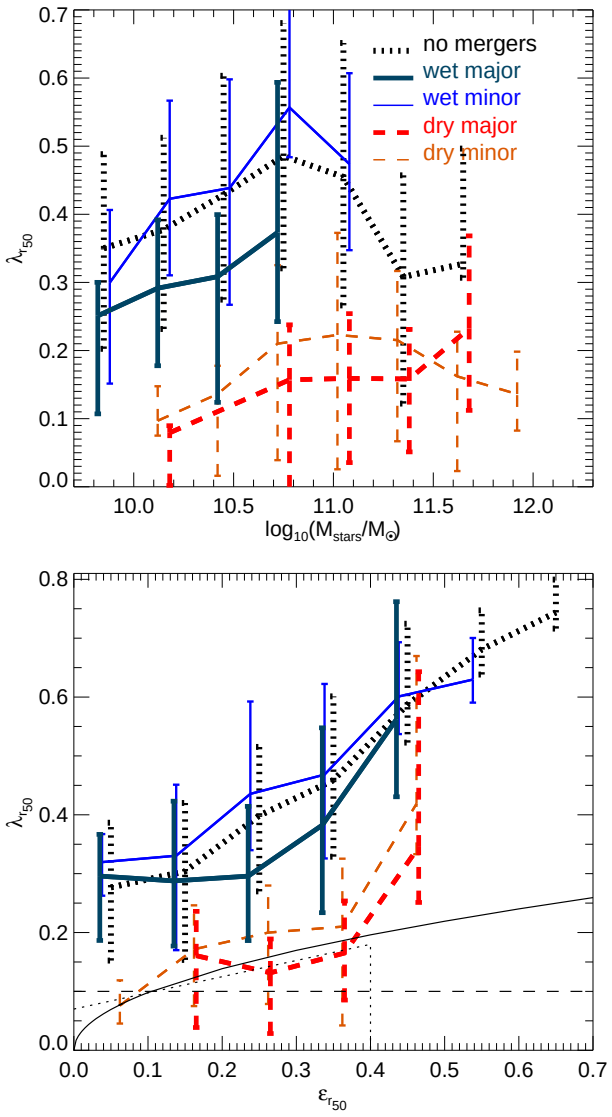

Figure 10. $\lambda_{r_{50}}$ as a function stellar mass (top panel) and $\epsilon_{r_{50}}$ (bottom panel) for galaxies with $M_{\rm stars} > 5{\times}10^9$ M$_\odot$ in the Ref-L100N1504 simulation at $z = 0$. Lines with error bars show the medians and $25^{\rm th} - 75^{\rm th}$ percentiles, respectively, for different samples of galaxies with different merger histories. The latter is shown only for bins with $\geqslant$ 5 galaxies. The samples correspond to galaxies that have not experienced mergers (thick dotted line), and that experienced at least one minor wet (thin solid line), minor dry (thin dashed line), major wet (thick solid line) and major dry (thick dashed line) merger in the last 10 Gyr. In the case of minor mergers we selected galaxies that did not have any major mergers in the last 10 Gyr. Here the separation between wet and dry merger is at $R_{\rm gas,merger} = 0.1$ (see Eq. 6 for a definition). There is a clear connection between dry mergers (either major or minor) with slow rotation kinematics at $M_{\rm stellar} > 10^{10}$ M$_\odot$.

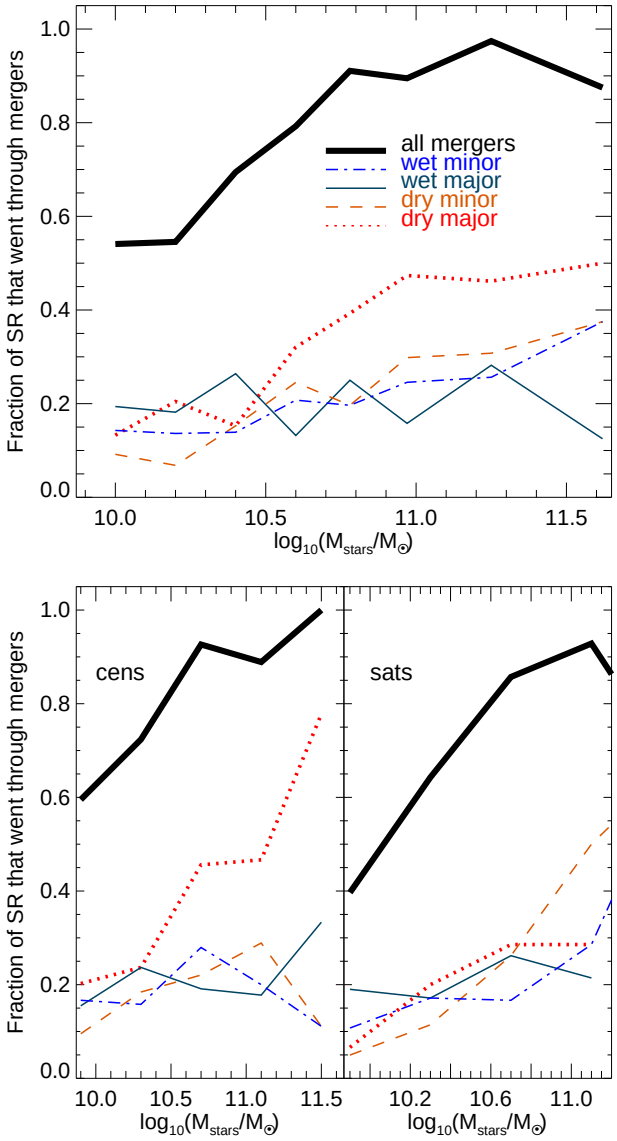

Figure 11. *Top panel:* Fraction of slow rotators at $z = 0$ in the Ref-L100N1504 simulation that suffered any type of mergers (thick solid line), and that have had at least one major dry (dotted line), major wet (thin solid line), minor dry (dashed line) or minor wet mergers (dot-dashed line), over the last 10 Gyr, as a function of their $z = 0$ stellar mass. We adopt the slow rotator classification of Cappellari (2016). *Bottom panel:* As in the top panel but split into central (left) and satellite (right) galaxies. Note that the x-axis in the panel of satellites spans a smaller dynamic range. This is because there are very few satellite galaxies with masses above 10^{11} M$_\odot$.

if any. Second, we analyse the effect that individual merging events have on $\lambda_{\rm R}$ and ϵ by comparing the kinematic properties of the main progenitors and merger remnants. Lagos et al. (2018) analysed the merger history of galaxies in the Ref-L100N1504 simulation, adding information on the cold gas masses of merging galaxies, orientation of mergers, orbital angular momentum and mass ratios. We use this extended merger catalogue to study the connection between mergers and slow rotation. Thus, here we focus solely on the Ref-L100N1504 simulation. We classify mergers as dry ($R_{\rm gas,merger} \leqslant 0.1$), wet ($R_{\rm gas,merger} > 0.1$), major (secondary to primary stellar mass ratio, $m_{\rm s}/m_{\rm p} \geqslant 0.3$) and minor ($0.1 \leqslant m_{\rm s}/m_{\rm p} < 0.3$; see § 2.2).

We take all galaxies at $z = 0$ in the Ref-L100N1504 simulation and split them into 5 samples: (i) galaxies that have not suffered mergers, those that have not suffered major mergers, but have suffered either (ii) dry or (iii) wet minor mergers, and those that have had major mergers either (iv) dry or (v) wet. Galaxies that

suffered major mergers could have also suffered minor mergers, but from the samples of minor mergers we remove all galaxies that had at least 1 major merger. This is done under the premise that major mergers have a more important effect on galaxy properties than minor mergers. This is supported by our previous results (Lagos et al. 2018). Our selection is based on the merger history of galaxies over the last 10 Gyr (i.e. approximately since $z = 2$).

Fig. 10 shows the median $\lambda_{\rm r50}$ as a function of $M_{\rm stars}$ and $\epsilon_{\rm r50}$ for galaxies at $z = 0$ that have $M_{\rm stars} > 5 \times 10^9\,{\rm M}_\odot$, separated in the 5 samples above, i.e. depending on their merger history. Here we do not distinguish between recent or far in the past mergers, but simply count their occurrence. We see a clear connection between the incidence of dry mergers (either major or minor) with slow rotation in galaxies with $M_{\rm stars} > 10^{10}\,{\rm M}_\odot$. On average, galaxies that went through dry major mergers have a lower $\lambda_{\rm r50}$ than those that went through dry minor mergers. The remnants of wet major mergers also tend to have relatively low $\lambda_{\rm r50}$, but not enough to place them on the slow rotation class, though $\approx 10\%$ of the wet major merger sample are slow rotators. Galaxies that had wet minor mergers have slightly larger $\lambda_{\rm r50}$ at fixed $\epsilon_{\rm r50}$ than galaxies that have not had mergers, possibly reflecting the fact that the former are on average a lot more gas rich (average neutral gas to stellar mass ratio of 19% compared to 6% in the latter sample). In Lagos et al. (2017) we showed, also using EAGLE, that continuous gas accretion and star formation efficiently spin up galaxies because the angular momentum brought by newly accreted gas is expected to grow proportionally with time (Catelan & Theuns 1996). Regardless of this effect, we find that the parameter space of $\lambda_{\rm r50} \gtrsim 0.7$ and $\epsilon \gtrsim 0.6$ is almost exclusively occupied by galaxies that have not had any mergers.

The fact that wet minor mergers appear to only slightly affect galaxies agrees with the conclusions of Lagos et al. (2018), in which it was shown that galaxies undergoing wet minor mergers have angular momentum radial profiles similar to galaxies that have not had mergers. The exception is the very centres of those galaxies, as the remnants of wet minor mergers tend to have slightly more massive bulges (see their Fig. 6). Although there is a clear trend between how galaxies populate the $\lambda_{\rm r50} - M_{\rm stars}$ and $\lambda_{\rm r50} - \epsilon_{\rm r50}$ planes and their merger history, the scatter is large, suggesting that mergers result in a plethora of remnants with no unique outcome. Our results support the findings of Naab et al. (2014) though with ≈ 50 times more mergers, which allows us to disentangle preferred formation mechanisms.

To disentangle the formation paths of slow rotators in EAGLE, we focus on their merger history as a function of stellar mass. The top panel of Fig. 11 shows the fraction of slow rotators that went through the 4 merging scenarios described above (wet/dry minor mergers, wet/dry major mergers), as a function of stellar mass at $z = 0$. We also show as black lines the fraction of slow rotators that had any form of merger with $m_{\rm s}/m_{\rm p} \geqslant 0.1$. We define slow rotators using the Cappellari (2016) criterion.

At $10^{10}\,{\rm M}_\odot \lesssim {\rm M}_{\rm stars} \lesssim 5 \times 10^{10}\,{\rm M}_\odot$, *$\approx 42\%$ of slow rotators have not had any mergers*. This percentage decreases systematically with increasing stellar mass, and by $M_{\rm stars} \approx 10^{11.5}\,{\rm M}_\odot$, 90% of the slow rotators had at least one merger during their past 10 Gyr. Among the slow rotators that had mergers, the most common type of merger is dry major merger, followed by minor mergers and wet major mergers.

In the bottom panel of Fig. 11 we separate centrals and satellites. The prevalence of dry major mergers is more significant in central galaxies. Here, dry major mergers are twice more common in slow rotators than the other forms of mergers. For satellites we see that the different types of mergers have a similar incidence and dry minor or major mergers become only slightly more prevalent at $M_{\rm stars} \gtrsim 10^{10.5}\,{\rm M}_\odot$. This shows that the importance of mergers and their type for slow rotation may have an environmental dependence. Nevertheless, there is a clear connection between dry mergers and slow rotators, but we still need to establish whether there is a causal connection between the two. We come back to this in § 4.1 where we analyse the effect of individual merger events on $\lambda_{\rm R}$ and $\epsilon_{\rm r50}$.

In Fig. 12 we show the history of $\lambda_{\rm r50}$ of galaxies that at $z = 0$ are classified as slow rotators. For the latter we apply a simple cut

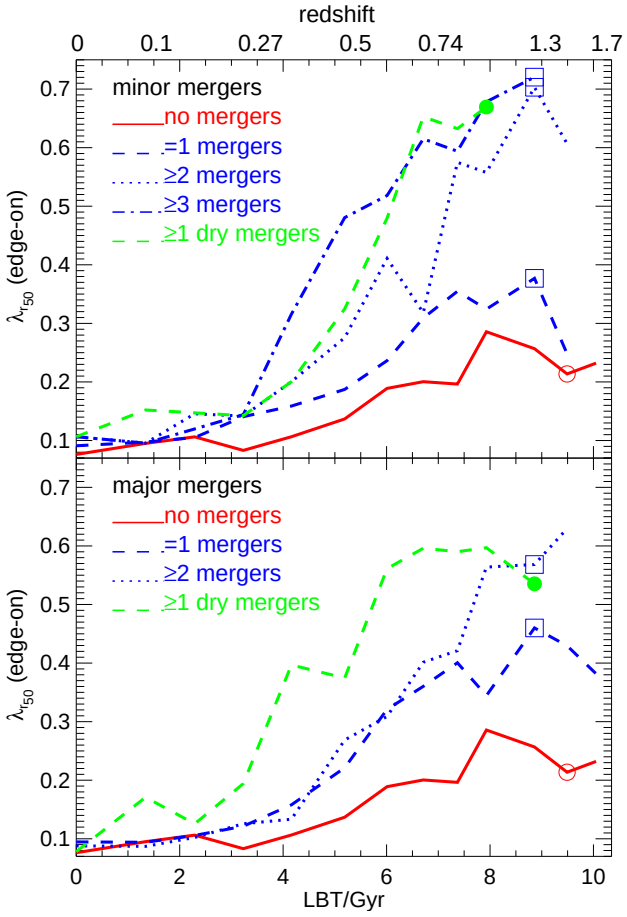

Figure 12. *Top panel:* Median $\lambda_{\rm r50}$ history of galaxies classified as slow rotators at $z = 0$ that have $M_{\rm stars} \geqslant 10^{10}\,{\rm M}_\odot$ in the Ref-L100N1504 simulation and that experienced only minor or no mergers. Here $\lambda_{\rm r50}$ was measured orienting galaxies edge-on. We show the history of these galaxies split into 5 samples: (i) slow rotators that have not experienced a merger (solid line), (ii) slow rotators that experienced one merger (blue dashed line), (iii) at least two mergers (blue dotted line), (iv) at least 3 mergers (blue dot-dashed line), and (v) at least one dry merger (green dashed line), as labelled. In the case of samples (ii), (iii) and (iv) we do not distinguish by the gas fraction of the merger, while in the case of (v) we impose a merger gas to stellar mass ratio threshold of 0.1 (see Eq. 6 for a definition). For reference, symbols show the median mass-weighted stellar age of the galaxies in each sample. *Bottom panel:* As in the top panel but for slow rotators that experienced major mergers. In this case the progenitors of these slow rotators could have also experienced minor mergers. Here we show samples (i), (ii), (iii) and (v) because major mergers are less frequent and thus, the sample of galaxies with $\geqslant 3$ major mergers is too small (6 **galaxies**).

of $\lambda_{r_{50}} \leqslant 0.1$ (Emsellem et al. 2007). To make the interpretation easier, we show the history of $\lambda_{r_{50}}$ measured after orienting galaxies edge-on (i.e. $\lambda_{r_{50}}$ takes its maximum value). We separate slow rotators that have only had minor mergers (top panel), and that have had major mergers (bottom panel). The latter could also have had minor mergers. In addition to minor and major mergers, we distinguish between different numbers of mergers (either wet or dry), and also show separately the slow rotators that had dry mergers. Symbols show the median mass-weighted stellar age of the galaxies in the different samples. Slow rotators that have not experienced any minor or major mergers were born with low $\lambda_{r_{50}}$ values, and at a look-back time of 8.5 Gyr, which is roughly the median mass-weighted stellar age of all these galaxies, they have $\lambda_{r_{50}}$ at least twice smaller than the rest of the galaxies. This is driven by the environments in which these galaxies formed. We come back to this in § 4.2.

The top panel of Fig. 12 shows that there is a cumulative effect of minor mergers, in which galaxies could have started with a high $\lambda_{r_{50}}$ but lost it through successive minor merger events. Note that those slow rotators that only had one minor merger, started with relatively low $\lambda_{r_{50}}$. The subsample of slow rotators that has had at least one dry minor merger shows the most dramatic evolution of $\lambda_{r_{50}}$ **(i.e. the fastest decrease)**, again supporting our conclusion that dry mergers are most effective at producing slow rotators. **In the case of galaxies having $\geqslant 3$ minor mergers in their history, a fast decrease of $\lambda_{r_{50}}$ is also seen, but this sample includes only 13 galaxies at $z = 0$.** Penoyre et al. (2017) recently analysed the Illustris simulation and concluded that they do not see a cumulative effect of minor mergers, in contradiction with the findings of Naab et al. (2014) and our results here. Given how sensitive the outcome of mergers are to their gas fraction (see § 4.1), one possible explanation to the different findings is that EAGLE produces a different gas fraction evolution of galaxies compared to Illustris, impacting the effect mergers have on galaxies. However, because the nature of these simulations is complex, with many processes acting simultaneously at any one time, it is hard to conclusively say what drives the differences between EAGLE and Illustris.

The bottom panel of Fig. 12 shows that **single** major mergers generally have a stronger effect than **single** minor mergers on the history of $\lambda_{r_{50}}$. This is clear when comparing the dashed lines between the top and bottom panels of Fig. 12, where galaxies that went through one major merger started with $\lambda_{r_{50}} \approx 0.45$, on average, while those that went through one minor merger started with $\lambda_{r_{50}} \approx 0.35$, on average. Major mergers also display a cumulative effect, but given how much rarer they are compared to minor mergers (see Fig. 2 in Lagos et al. 2018), the significance of this is minimal for the entire galaxy population; i.e. there are only 11 galaxies in the entire simulated volume that had $\geqslant 2$ major mergers in the last 10 Gyr. When selecting slow rotators that had at least one dry major merger, we see a much more drastic decrease in $\lambda_{r_{50}}$. In § 4.1 we show that dry mergers are connected with the most significant decrease in $\lambda_{r_{50}}$ in individual merger events.

For both minor and major mergers, we see that slow rotators that went through dry mergers, experience a rapid decrease of $\lambda_{r_{50}}$ at look-back times $\lesssim 6$ Gyr. This is due to the dry merger rate increasing rapidly after that epoch towards $z = 0$. On the other hand, the total merger rate decreases smoothly, which explains why the $\lambda_{r_{50}}$ evolutionary tracks of galaxies that suffered one or two mergers display a smoother decrease.

The fact that all the galaxies that at $z = 0$ are slow rotators display an overall spin down throughout their lives even in the absence of mergers, is probably connected to the evolution of the local environment in which galaxies and halos reside. Welker et al. (2015) show that halos, as they move from high-vorticity regions in the cosmic web towards the filaments and nodes, start to be subject to less and less coherent gas accretion. In the limit of nodes in the cosmic web, accretion happens a lot more isotropically than in the high-vorticity regions or filaments, with several filaments connecting to the node from different directions. High-vorticity regions accrete gas from preferential directions, thus gaining more coherent angular momentum. The overall spin down we see in massive galaxies and halos (see § 4.2) is most likely linked to the overall environmental evolution. Fast rotators do not necessarily experience the same spin down because they tend to inhabit lower mass halos, which are less clustered.

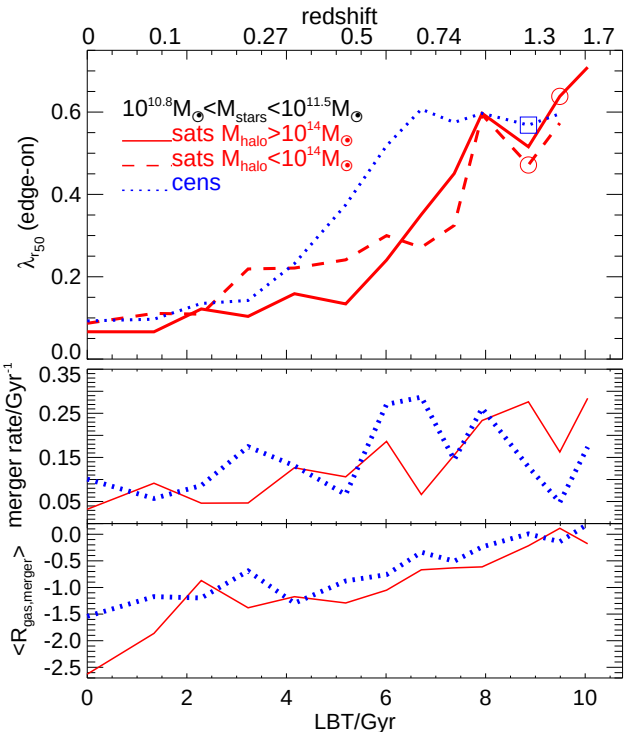

Figure 13. *Top panel:* **Median $\lambda_{r_{50}}$ history of galaxies that at $z = 0$ have $\lambda_{r_{50}} \leqslant 0.1$ and $10^{10.8}\,M_\odot < M_{stars} < 10^{11.5}\,M_\odot$ in the Ref-L100N1504 simulation. We separate galaxies in this mass bin into satellites that at $z = 0$ are hosted by halos of masses above (solid line) and below (dashed line) $10^{14}\,M_\odot$, and centrals (dashed line). Symbols show the median mass-weighted stellar age of the galaxies in each sample.** *Middle panel:* **merger rate of the galaxies in the top panel, separating into centrals and satellites.** *Bottom panel:* **median neutral gas-to-stellar mass ratio of the mergers in the middle panel.**

In § 3 we showed that satellites are 25% more likely to be slow rotators than centrals at $M_{stars} \gtrsim 10^{10.8}\,M_\odot$. Fig. 11 shows that at $10^{10.8}\,M_\odot < M_{stars} < 10^{11.5}\,M_\odot$, satellite galaxies have a higher merger incidence than centrals (92% vs. 87%). Thus, it is natural to expect massive satellites to have a higher F_{SR}. The top panel of Fig. 13 shows that satellites that at $z = 0$ are slow rotators, spun down earlier (at look-back times < 8 Gyr) and have older stellar populations than centrals (which spun down at < 6 Gyr), at fixed stellar mass. The latter becomes exacerbated in satellites of halos with masses $> 10^{14}\,M_\odot$. The middle panel of Fig. 13 shows that this earlier spinning down is due to the satellite merger rate peaking at

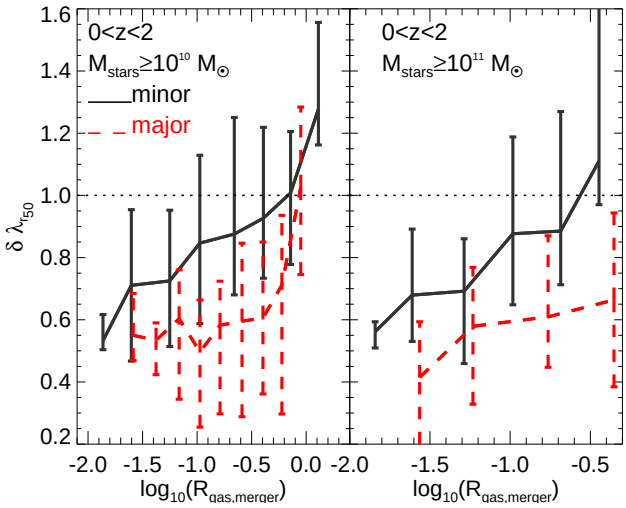

Figure 14. Variation of $\lambda_{\rm r}$ measured at r_{50} as a function of the gas to stellar mass ratio of the merger (see Eq. 6) separating minor and major mergers, as labelled. The left panel shows all the mergers that took place in galaxies with $M_{\rm stars} \geqslant 10^{10}\,{\rm M}_{\odot}$ at $0 \leqslant z \leqslant 2$, while the right panel shows the subsample of galaxies with $M_{\rm stars} \geqslant 10^{11}\,{\rm M}_{\odot}$. Lines with error bars show the median and $25^{\rm th} - 75^{\rm th}$ percentile ranges. Only bins with $\geqslant 5$ objects are shown. For reference, the dotted horizontal line shows no change in $\lambda_{\rm r}$. Positive values indicate the merger remnant has a higher value of $\lambda_{\rm r}$ than the progenitor.

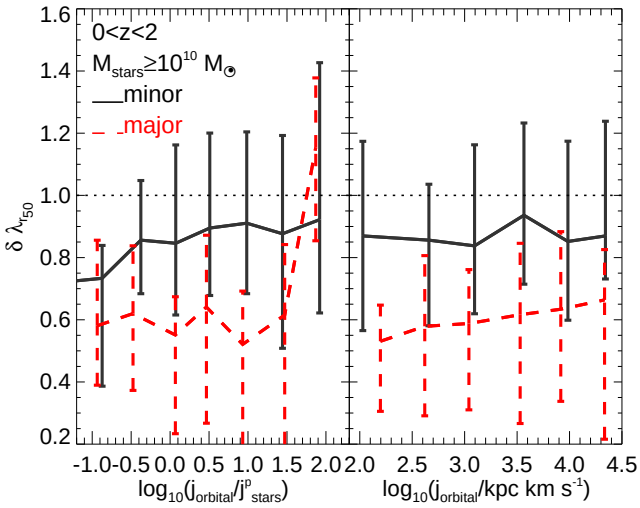

Figure 15. $\delta\,\lambda_{\rm R}$ as a function of the ratio between the orbital and stellar specific angular momentum of the primary galaxy (left panel), and the orbital specific angular momentum (right panel), for all the mergers that took place in galaxies with $M_{\rm stars} \geqslant 10^{10}\,{\rm M}_{\odot}$ at $0 \leqslant z \leqslant 2$. We separate minor and major mergers, as labelled.

higher redshifts than centrals. In addition, the galaxy mergers suffered by the population of satellite slow rotators at $z = 0$ is lower than centrals, on average. As the merger gas fraction is correlated with the resulting change in $\lambda_{\rm R}$ (which we show in § 4.1) it is expected that the satellite mergers have a more devastating effect on $\lambda_{\rm R}$, on average, than the mergers centrals experience.

4.1 The effect of individual merger events on $\lambda_{\rm R}$

In order to determine the effect that individual mergers have on the rotation of galaxies, we take all the minor and major mergers that have primary galaxies with $M_{\rm stars} \geqslant 10^{10}\,{\rm M}_{\odot}$ from $z = 0$ to $z = 2$, and compute the change in $\lambda_{\rm R}$ before and after the merger. Note that here we do not distinguish between descendants that are slow/fast rotators, but take all mergers. We then compare $\lambda_{\rm R}$ between the main progenitor (the most massive) in the last snapshot the two merging galaxies were identified individually and the merger remnant. The latter corresponds to the first snapshot in which the two galaxies appear merged. Typically the timescale between these snapshots is ≈ 0.5 Gyr. We define

$$\delta\,\lambda_{\rm R} = \frac{\lambda_{\rm R,rem}}{\lambda_{\rm R,prog}}, \qquad (8)$$

with $\lambda_{\rm R,rem}$ and $\lambda_{\rm R,prog}$ being the remnant's and main progenitor's $\lambda_{\rm R}$, respectively.

Fig. 14 shows $\delta\,\lambda_{\rm r_{50}}$ (measured at r_{50}) as a function of the cold gas to stellar mass ratio of the merger, $R_{\rm gas,merger}$ (Eq. 6). We show minor and major mergers separately. The right panel of Fig. 14 shows the subsample of galaxies with $M_{\rm stars} \geqslant 10^{11}\,{\rm M}_{\odot}$. There is a positive correlation between $\delta\,\lambda_{\rm r_{50}}$ and $R_{\rm gas,merger}$, **but with an offset in normalization in a way that major mergers are 25% more likely to decrease $\lambda_{\rm R}$ compared to minor mergers. Major mergers also do this to a greater extent than minor mergers, decreasing $\lambda_{\rm R}$ by 39% compared to 12% in the latter, on average.** Galaxy minor **(major)** mergers with $R_{\rm gas,merger} \gtrsim 0.5$ (0.8) have a clear preference for increasing $\lambda_{\rm R}$, while those with $R_{\rm gas,merger} \lesssim 0.1$ have a **strong** preference for decreasing $\lambda_{\rm R}$. However, the scatter around the median relation is large, suggesting that the effect of a merger on $\lambda_{\rm R}$ is not uniquely determined by its mass ratio and gas fraction. Penoyre et al. (2017) found in Illustris that major mergers, regardless of their gas fraction, are connected with the spinning down of galaxies, in contradiction with our findings. This may be due to their major mergers being mostly gas poor (gas-to-stellar mass ratios $\lesssim 0.1$; see their Fig. 13), thus, lacking the very gas-rich major mergers we obtain in EAGLE that spin up galaxies ($R_{\rm gas,merger} \gtrsim 0.8$).

Focusing specifically on dry mergers ($R_{\rm gas,merger} \leqslant 0.1$), we find that in ≈ 15% of the major mergers $\lambda_{\rm R}$ increases, while for minor mergers this fraction is 25%. Selecting only massive galaxies in EAGLE (right panel in Fig. 14) does not change the correlation between $\delta\,\lambda_{\rm r_{50}}$ and $R_{\rm gas,merger}$ significantly. We analysed $\delta\,\lambda_{\rm 2r_{50}}$ (measured at $2\,r_{50}$) and found a very similar relation to that shown in Fig. 14. This suggests that mergers modify $\lambda_{\rm R}$ in a similar fashion over a large radial range. It is clear that the high incidence of dry major mergers in the slow rotator population of Fig. 11 is due to these mergers having a detrimental effect on $\lambda_{\rm R}$, on average.

Fig. 15 shows $\delta\,\lambda_{\rm R}$ as a function of $j_{\rm orbital}/j^{\rm p}_{\rm stars}$ (left panel) and $j_{\rm orbital}$ (right panel). Here, $j^{\rm p}_{\rm stars}$ is the total stellar specific angular momentum of the primary galaxy. In major mergers the orbital angular momentum has an effect on $\lambda_{\rm R}$, which is more clearly seen when we study $j_{\rm orbital}/j^{\rm p}_{\rm stars}$, in a way that high $j_{\rm orbital}$ drives smaller changes in $\lambda_{\rm R}$. Minor mergers display a much weaker dependence on $j_{\rm orbital}/j^{\rm p}_{\rm stars}$ and no clear dependence on $j_{\rm orbital}$. We also studied the effect of alignments of the rotation axis of the merger pair and found no effect on $\lambda_{\rm R}$ (not shown here).

Li et al. (2018) analysed the effect of the merger orbits on

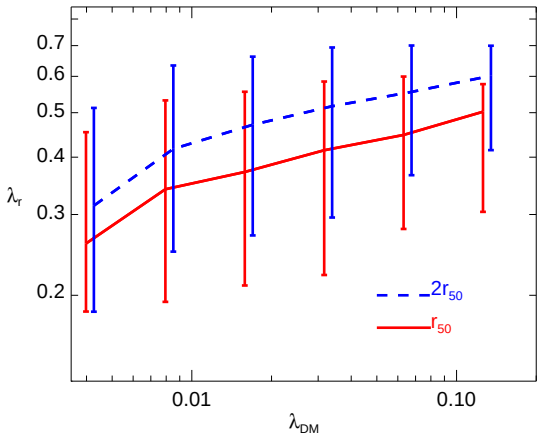

Figure 16. $\lambda_{\rm R}$ measured within r_{50} and $2r_{50}$, as labelled, as a function of the dark matter halo λ (Eq. 9) for central galaxies in EAGLE at $z = 0$ that have $M_{\rm stars} \geqslant 10^{10}\,{\rm M}_{\odot}$. Lines with error bars show the median and $16^{\rm th} - 84^{\rm th}$ percentile ranges, respectively.

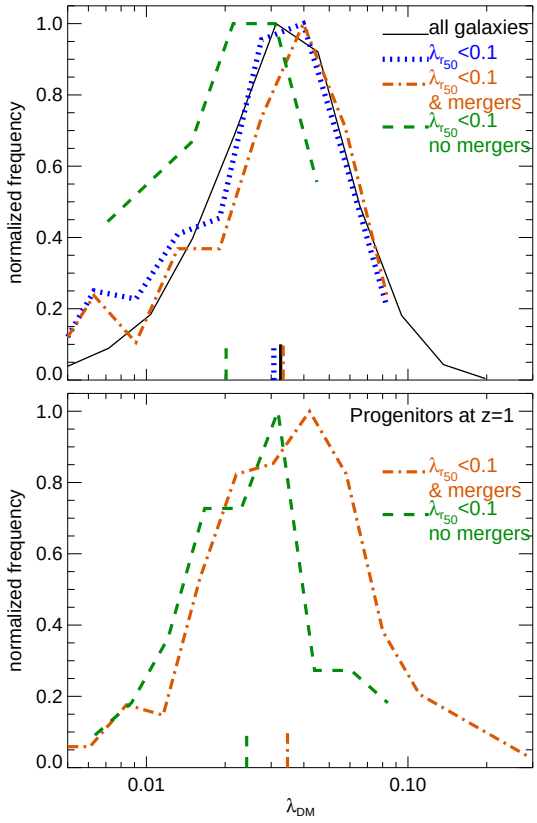

Figure 17. *Top panel:* The dark matter halo λ for central galaxies in EAGLE at $z = 0$ that have $M_{\rm stars} \geqslant 10^{10}\,{\rm M}_{\odot}$. Four subsamples are presented: all galaxies (solid line), those with $\lambda_{\rm r_{50}} < 0.1$ (dotted line), those with $\lambda_{\rm r_{50}} < 0.1$ and that had at least 1 merger in the last 10 Gyr (dot-dashed line), and those with those with $\lambda_{\rm r_{50}} < 0.1$ that have not had any mergere in the same period of time (dashed line). *Bottom panel:* As in the top panel but for the progenitor halos at $z = 1$ of the two populations of slow rotators at $z = 0$: (i) those that experienced mergers, and (ii) those that did not. We find that the host halos of slow rotators that at $z = 0$ have not yet experienced mergers, are biased towards low spins even at $z = 1$.

the shape and $\lambda_{\rm R}$ of merger remnants using the Illustris simulation, and found that circular orbits tend to produce fast rotators, while radial orbits produce slow rotators. In our calculation, radial orbits correspond to low $j_{\rm orbital}$, and in agreement with Li et al., we find that the decrease in $\lambda_{\rm R}$ is the largest in these cases. However, the scatter around the median is very large, and the dependence on $R_{\rm gas,merger}$ is stronger. This agrees with the conclusion of Lagos et al. (2018), who showed that the gas fraction of the merger is the most fundamental property determining the effect on the angular momentum of the merger remnant in EAGLE, with the mass ratio modulating the strength of the effect.

We find that in the absence of mergers, galaxies display little change in their $\lambda_{\rm R}$, $< 5\%$. This seems to contradict the result of Choi & Yi (2017), who argued that most of the spin down of galaxies is driven by environment and not mergers. This could be due to their study being performed exclusively on cluster regions, which represent an upper limit for the effect of environment.

We also studied the effect of mergers on the ellipticity, ϵ, of galaxies and found little effect (not shown here). Dry mergers have a tendency to increase ϵ, which, combined with the fact that they tend to decrease $\lambda_{\rm R}$, results in galaxies ending up more comfortably in the slow rotator zone in the $\lambda_{\rm R} - \epsilon$ plane. On the other hand, wet major mergers tend to decrease ϵ, thus making galaxies rounder. This is expected since wet mergers tend to increase the central stellar density of galaxies due to efficient gas fueling to the centre (e.g. Cox et al. 2006;Robertson et al. 2006; Johansson et al. 2009; Peirani et al. 2010; Moreno et al. 2015; Lagos et al. 2018).

4.2 The connection between slow rotators and the halo spin parameters

Fig. 11 showed that about 30% of the slow rotator population in the Ref-L100N1504 have not had any mergers. Fig. 12 showed that these slow rotators also had modest $\lambda_{\rm r_{50}}$ in the past, smaller than the $\lambda_{\rm r_{50}}$ values of the progenitors of slow rotators that experienced mergers. Here, we study the halos of these galaxies to understand why they are slow rotators.

We calculate the spin of halos, $\lambda_{\rm DM}$, as in Mo et al. (1998),

$$\lambda_{\rm DM} = j_{\rm h}\,\frac{(10\,H)^{1/3}}{\sqrt{2}\,G^{2/3}}\,M_{\rm h}^{-2/3} \qquad (9)$$

where $j_{\rm h}$ and $M_{\rm h}$ are the halo specific angular momentum and dark matter M_{200} mass[1], respectively, G is Newton's gravity constant and H is the Hubble parameter. We calculate $j_{\rm h}$ with all the dark matter particles within a halo's r_{200}. We find a positive correlation between between the stellar $\lambda_{\rm R}$ and $\lambda_{\rm DM}$ in central galaxies (Fig. 16), but with significant scatter. Interestingly, this scatter tends to decrease with increasing aperture within which $\lambda_{\rm R}$ is measured.

We now focus only on slow rotators to investigate the possible connection with their host halo spin. The top panel of Fig. 17 shows the distribution of halo dark matter spin parameters, $\lambda_{\rm DM}$, of all central galaxies in the Ref-L100N1504 at $z = 0$ that have stellar masses $> 10^{10}\,{\rm M}_{\odot}$ (solid line). In the top panel of Fig. 17 we also show central galaxies with $\lambda_{\rm r_{50}} < 0.1$ (dashed line), and

[1] Measured with all the dark matter particles within the halo's r_{200}, the radius within which the density is $200\,\rho_{\rm crit}$, with $\rho_{\rm crit}$ being the critical density.

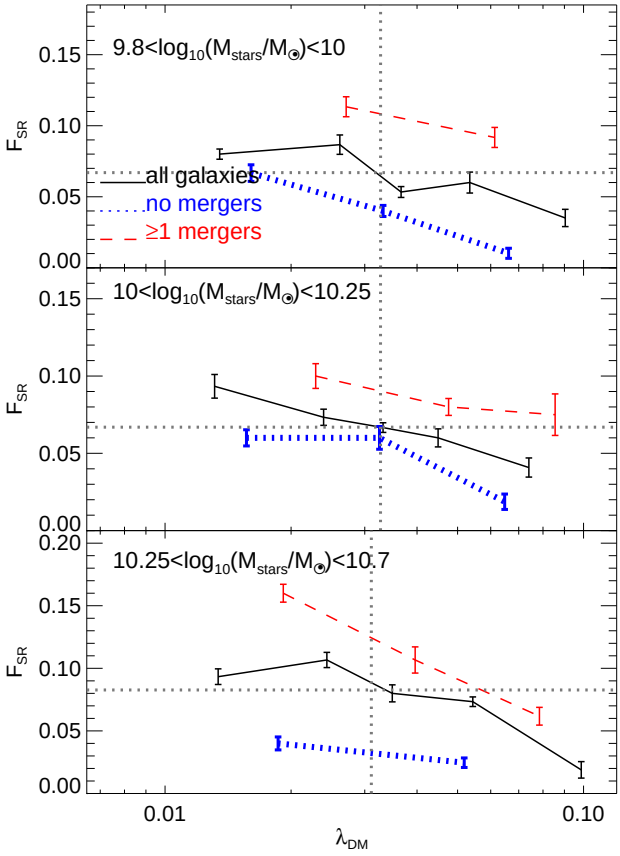

Figure 18. The fraction of central galaxies that are slow rotators at $z = 0$ (defined as those with $\lambda_{\rm r_{50}} \leqslant 0.1$) as a function of the halo spin parameter, $\lambda_{\rm DM}$, in three bins of stellar mass of the central galaxy, as labelled in each panel. We show this for 3 samples: all central galaxies (solid line), and the subsamples that had at least 1 merger (dashed line) or no mergers (dotted line). Bins are chosen to have $\approx$ 150 galaxies. Error bars correspond to 1 standard deviation calculated with 10 jackknife resamplings in individual mass bins. The horizontal and vertical line shows the fraction of slow rotators for all galaxies at $z = 0$ in the stellar mass bins and their median $\lambda_{\rm DM}$. There is a clear tendency for low λ halos to have a higher fraction of slow rotators.

the subsamples of these slow rotators that have had mergers (dot-dashed line) and had not had minor/major mergers (dashed line) over the last 10 Gyr. Slow rotators that have not had mergers display a $\lambda_{\rm DM}$ distribution that is significantly shifted compared to the other 3 samples. Note that the median $\lambda_{\rm DM}$ of galaxies with $\lambda_{\rm r_{50}} < 0.1$ that have had mergers is very similar to the overall population of central galaxies. The sample of centrals with $\lambda_{\rm r_{50}} < 0.1$ has a slightly smaller median, but that is caused by the contribution of centrals with $\lambda_{\rm r_{50}} < 0.1$ that have not had mergers. The latter is clear when comparing the slow rotators that have had mergers to the overall galaxy population (dot-dashed and solid lines in the top panel of Fig. 17). The median $\lambda_{\rm DM}$ of slow rotators that have not experienced mergers is a factor of ≈ 2 smaller. This explains why they formed with low $\lambda_{\rm r_{50}}$ values: they formed and evolved in halos of low spins. On average, galaxies and their host halos grow their angular momentum together in a way that resembles weak conservation of angular momentum (Mo et al. 1998; Zavala et al. 2016; Lagos et al. 2017), and so it is expected that low spin halos preferentially lead to the formation of galaxies with low spins.

The bottom panel of Fig. 17 shows the distribution of spin parameters of the $z = 1$ halos that contain the progenitors of the slow rotators at $z = 0$. This shows that the spins of the halos hosting the slow rotators that never had mergers were already low 7 Gyr ago, preventing the galaxies from reaching significant $\lambda_{\rm R}$. Interestingly, we see that on average the halos hosting these galaxies decrease their $\lambda_{\rm DM}$ from $\approx$ 0.025 to 0.02 from $z = 1$ to $z = 0$, which may be the cause for the systematic spinning down displayed by the slow rotators that never had mergers (solid lines in Fig. 12).

There is an overall weak positive correlation between $\lambda_{\rm r_{50}}$ and $\lambda_{\rm DM}$ for central galaxies (Fig. 16). However, when studying the incidence of slow rotators, a stronger correlation with $\lambda_{\rm DM}$ emerges. This is investigated in Fig. 18 for central galaxies in the Ref-L100N1504 simulation at $z = 0$ in three bins of stellar mass. The average $F_{\rm SR}$ of all central galaxies is shown as the solid line, while the subsamples of galaxies that had mergers and those that did not have mergers are shown as dashed and dotted lines, respectively. The stellar mass bins were chosen to have > 500 galaxies in each of the three samples above.

The dependence of $F_{\rm SR}$ on $\lambda_{\rm DM}$ is close to monotonic with $F_{\rm SR}$ decreasing with increasing $\lambda_{\rm DM}$. We find that galaxies that have had mergers at $z < 2$ have a higher $F_{\rm SR}$ compared to galaxies that have not had mergers at fixed $\lambda_{\rm DM}$. The correlation is similarly tight for the different samples; i.e. jackknife errors are of a similar magnitude regardless of the merger history of galaxies. The top and middle panels of Fig. 18 shows that galaxies that have not had mergers and are hosted by halos of low $\lambda_{\rm DM}$, have a $F_{\rm SR}$ that is similar or higher than that of the overall galaxy population at that stellar mass. Our results show the importance of the halo spin in determining slow rotation in central galaxies.

5 DISCUSSION AND CONCLUSIONS

Recent observational results from IFS surveys have reached contradictory conclusions regarding the effect of environment on the frequency of slow rotators. The early work from ATLAS$^{\rm 3D}$ (Cappellari et al. 2011) concluded that the fraction of slow rotators increases steeply with stellar mass and towards denser environments (Emsellem et al. 2011). However, recent surveys that sample much larger numbers of galaxies have concluded that there is only a very weak or no dependence on environment once stellar mass is controlled for (Brough et al. 2017; Veale et al. 2017b; Greene et al. 2017). Here we used the EAGLE and HYDRANGEA simulations to explore this question and shed light onto the formation mechanisms of slow rotators.

We took special care in constructing IFS-like cubes for all of our simulated galaxies to measure the relevant quantities, $\lambda_{\rm R}$ and ϵ, in a way that is more directly comparable to observations. We classify galaxies in EAGLE and HYDRANGEA that have stellar masses $> 5 \times 10^9\,{\rm M}_\odot$ into slow and fast rotators, using several observational criteria. We compare with the observations of Emsellem et al. (2011), Brough et al. (2017) and Veale et al. (2017b) and find that our simulations reproduce the dependence of the fraction of slow rotators, $\rm F_{SR}$, on stellar mass relatively well. We showed that by applying small offsets to the observational classifications we recover excellent agreement with the observations at $M_{\rm stars} \lesssim 10^{11.5}\,{\rm M}_\odot$ (Fig. 5). At higher masses, we find a low frequency of slow rotators, $\approx 20\%$, while observations point to a much higher fraction $> 50\%$ (Oliva-Altamirano et al. 2017; Brough et al. 2017). This discrepancy is likely due to BCGs in EAGLE and HYDRANGEA being overly massive for their halo mass and

have star formation rates that are higher than observations. Continuing star formation is very efficient at spinning up galaxies, resulting in BCGs being mostly fast rotators.

We explored the effect of environment in two ways: by separating centrals and satellites, and by studying the effect of halo mass on the distribution of galaxies in the $\mathrm{F_{SR}}$-stellar mass plane. We find that satellite galaxies are $49 \pm 15\%$ more likely to be slow rotators than centrals at stellar masses in the range $10^{10.8}\,\mathrm{M}_\odot - 10^{11.5}\,\mathrm{M}_\odot$. At lower masses we find little differences in the overall populations of satellies and centrals (Fig. 6). However, when focusing on the passive population, we find that centrals of masses $M_{\rm stars} \lesssim 10^{10.7}\,\mathrm{M}_\odot$ are twice as likely to be slow rotators than satellites are (Fig. 7). We interpret this as centrals undergoing quenching and morphological transformation simultaneously, while satellites can quench due to the environment they live in without changing morphology.

We separate satellites and centrals by the halo mass they reside in, and find a significant trend with halo mass for centrals galaxies, where $\mathrm{F_{SR}}$ increases with increasing halo mass at fixed stellar mass (top panel of Fig. 8). Satellite galaxies on the other hand show no dependence on halo mass once stellar mass in controlled for (bottom panel Fig. 8). However, the subsample of passive satellites shows a significant trend with halo mass, with $\mathrm{F_{SR}}$ increasing with decreasing halo mass at $M_{\rm stars} < 10^{10.5}\,\mathrm{M}_\odot$ (Fig. 9). We speculate that satellite galaxies in low-mass halos, $M_{\rm halo} \lesssim 10^{13}\,\mathrm{M}_\odot$, require morphological transformation to be quenched, while this is not the case in massive halos, $M_{\rm halo} \gtrsim 10^{14}\,\mathrm{M}_\odot$. Correa et al. (2017) presented an analysis of the connection between the bulge-to-total stellar mass ratio of EAGLE galaxies with their colours. The authors concluded that satellite galaxies in the red sequence are more morphologically diverse compared to centrals, consistent with satellites quenching without having to transform morphologically. Note that the latter may not hold for low-mass galaxies (here we are only analysing galaxies with stellar masses $> 5 \times 10^9\,\mathrm{M}_\odot$). These are predictions that should be testable with the full catalogues of MaNGA (Bundy et al. 2015) and SAMI (Bryant et al. 2015) in combination with high-quality group catalogues (Yang et al. 2007; Robotham et al. 2011; Saulder et al. 2016).

We use the extended merger tree information of EAGLE, as described in Qu et al. (2017) and Lagos et al. (2018), to study the formation history of simulated galaxies. We find that there is a strong correlation between slow rotation and the incidence of dry mergers. Most galaxies ($\approx 60\%$) that have had at least one dry major merger in the last 10 Gyr reside in the slow rotation region of the $\lambda_{\mathrm{r_{50}}}$-$\epsilon_{\mathrm{r_{50}}}$ plane. Less frequent, but nonetheless common among slow rotators, are dry minor mergers. Wet major and minor mergers are however more common in fast rotators (see Fig. 10). We find that the region of $\lambda_{\mathrm{r_{50}}} \gtrsim 0.7$ and $\epsilon_{\mathrm{r_{50}}} \gtrsim 0.6$ is almost exclusively occupied by galaxies that have not had any mergers with mass ratios $\geqslant 0.1$. Separating centrals and satellites, we find that dry major mergers are twice more common than any other merger with mass ratio $\geqslant 0.1$ in the population of central slow rotators, while for satellites dry minor and major mergers are the dominant form of mergers (Fig 11).

By studying individual merger events, we find that dry major and minor mergers tend to be associated with a net spin down of galaxies, while wet mergers can spin up galaxies very efficiently (Fig. 14). We find that mergers have a cumulative effect, and galaxies undergoing successive minor mergers are more likely to spin down and become slow rotators. For comparison, galaxies that had $\geqslant 3$ mergers have an incidence of slow rotators of 30%, while this fraction decreases to 10% in galaxies that had one merger (not shown here). **We also found a secondary effect of the orbital angular momentum on the remnant $\lambda_{\mathrm{r_{50}}}$ in the case of major mergers, in a way that lower orbital angular momentum leads to a larger decrease in $\lambda_{\mathrm{r_{50}}}$ (Fig. 15).** Surprisingly, $\approx 30\%$ of the slow rotators in EAGLE have not had mergers with mass ratios $\geqslant 0.1$. Those galaxies tend to have been born in halos of low spins (Fig. 17) and we find that they currently reside in halos with median spin at least twice smaller than the rest of the slow rotators and the overall galaxy population.

EAGLE shows that although the formation paths of slow rotators can be varied, as previously pointed out by Naab et al. (2014) using a small sample of 44 simulated galaxies, there are preferred formation mechanisms. Those are dry major mergers in the case of central galaxies, dry minor and major mergers in the case of satellites, and being formed in halos of small spins in the case of slow rotators that have not had mergers.

One limitation we found is that the most massive galaxies in EAGLE and HYDRANGEA, $M_{\rm stars} > 10^{11.5}\,\mathrm{M}_\odot$, are preferentially fast rotators, in contradiction with observations. This is connected to them being overly massive for their halo mass and star-forming (Bahé et al. 2017; Barnes et al. 2017). All these features are indicative of AGN feedback not being strong enough at the highest masses. In addition, EAGLE lacks the population of very flat galaxies, $\epsilon_{\mathrm{r_{50}}} > 0.7$. This is most likely due to the modelling of the ISM and cooling adopted in EAGLE, as gas is forced to not cool down below $\approx 8,000$ K, which corresponds to a Jeans length of ≈ 1 kpc, much larger than the scaleheights of disks in the local Universe (Kregel et al. 2002). This issue could be solved by including the formation of the cold ISM. This, however, does not affect the capability of our simulations to study slow rotators. Overall, our results show that simulations like EAGLE and HYDRANGEA are extremely powerful as their resolution allows us to look at their internal kinematics, at the same time as having large statistical samples to distinguish preferred formation scenarios.

ACKNOWLEDGEMENTS

The authors thank Eric Emsellem, Luca Cortese, Sarah Brough, Thorsten Naab and the theory and computing group at ICRAR for fruitful discussions. We also thank the anonymous referee for a constructive and helpful report. CL also thanks Rodrigo Tobar for the technical help. CL is funded by a Discovery Early Career Researcher Award (DE150100618). CL also thanks the MERAC Foundation for a Postdoctoral Research Award and Cardiff University for their visitor program. YB received funding from the European Union's Horizon 2020 research and innovation programme under the Marie Sklodowska-Curie grant agreement No 747645. STK and DB acknowledge support from STFC through grant ST/L000768/1. This work used the DiRAC Data Centric system at Durham University, operated by the Institute for Computational Cosmology on behalf of the STFC DiRAC HPC Facility (`www.dirac.ac.uk`). This equipment was funded by BIS National E-infrastructure capital grant ST/K00042X/1, STFC capital grant ST/H008519/1, and STFC DiRAC Operations grant ST/K003267/1 and Durham University. DiRAC is part of the National E-Infrastructure. Support was also received via the Interuniversity Attraction Poles Programme initiated by the Belgian Science Policy Office ([AP P7/08 CHARM]), the National Science Foundation under Grant No. NSF PHY11-25915, and the UK Science and Technology Facilities Council (grant numbers

ST/F001166/1 and ST/I000976/1) via rolling and consolidating grants awarded to the ICC. We acknowledge the Virgo Consortium for making their simulation data available. The EAGLE simulations were performed using the DiRAC-2 facility at Durham, managed by the ICC, and the PRACE facility Curie based in France at TGCC, CEA, Bruyeres-le-Chatel. This research was supported in part by the National Science Foundation under Grant No. NSF PHY11-25915. The Hydrangea simulations were in part performed on the German federal maximum performance computer HazelHen at the maximum performance computing centre Stuttgart (HLRS), under project GCS-HYDA / ID 44067 financed through the large-scale project Hydrangea of the Gauss Center for Supercomputing. Further simulations were performed at the Max Planck Computing and Data Facility in Garching, Germany. Parts of this research were conducted by the Australian Research Council Centre of Excellence for All-sky Astrophysics (CAASTRO), through project number CE110001020. This work was also supported by the Netherlands Organisation for Scientific Research (NWO), through VICI grant 639.043.409.

REFERENCES

Bacon R., Copin Y., Monnet G., Miller B. W., Allington-Smith J. R., Bureau M., Carollo C. M., Davies R. L. et al, 2001, MNRAS, 326, 23
Bahé Y. M., Barnes D. J., Dalla Vecchia C., Kay S. T., White S. D. M., McCarthy I. G., Schaye J., Bower R. G. et al, 2017, ArXiv e-prints
Bahé Y. M., Crain R. A., Kauffmann G., Bower R. G., Schaye J., Furlong M., Lagos C., Schaller M. et al, 2016, MNRAS, 456, 1115
Barnes D. J., Kay S. T., Bahé Y. M., Dalla Vecchia C., McCarthy I. G., Schaye J., Bower R. G., Jenkins A. et al, 2017, MNRAS, 471, 1088
Bois M., Bournaud F., Emsellem E., Alatalo K., Blitz L., Bureau M., Cappellari M., Davies R. L. et al, 2010, MNRAS, 406, 2405
Bois M., Emsellem E., Bournaud F., Alatalo K., Blitz L., Bureau M., Cappellari M., Davies R. L. et al, 2011, MNRAS, 416, 1654
Brough S., van de Sande J., Owers M. S., d'Eugenio F., Sharp R., Cortese L., Scott N., Croom S. M. et al, 2017, ArXiv e-prints
Bryant J. J., Owers M. S., Robotham A. S. G., Croom S. M., Driver S. P., Drinkwater M. J., Lorente N. P. F., Cortese L. et al, 2015, MNRAS, 447, 2857
Bundy K., Bershady M. A., Law D. R., Yan R., Drory N., MacDonald N., Wake D. A., Cherinka B. et al, 2015, ApJ, 798, 7
Cappellari M., 2016, ARA&A, 54, 597
Cappellari M., Emsellem E., Bacon R., Bureau M., Davies R. L., de Zeeuw P. T., Falcón-Barroso J., Krajnović D. et al, 2007, MNRAS, 379, 418
Cappellari M., Emsellem E., Krajnović D., McDermid R. M., Scott N., Verdoes Kleijn G. A., Young L. M., Alatalo K. et al, 2011, MNRAS, 413, 813
Catelan P., Theuns T., 1996, MNRAS, 282, 436
Choi H., Yi S. K., 2017, ApJ, 837, 68
Correa C. A., Schaye J., Clauwens B., Bower R. G., Crain R. A., Schaller M., Theuns T., Thob A. C. R., 2017, ArXiv:1704.06283
Cox T. J., Dutta S. N., Di Matteo T., Hernquist L., Hopkins P. F., Robertson B., Springel V., 2006, ApJ, 650, 791
Crain R. A., Bahe Y. M., Lagos C. d. P., Rahmati A., Schaye J., McCarthy I. G., Marasco A., Bower R. G. et al, 2016, ArXiv:1604.06803
Crain R. A., Schaye J., Bower R. G., Furlong M., Schaller M., Theuns T., Dalla Vecchia C., Frenk C. S. et al, 2015, MNRAS, 450, 1937
Croom S. M., Lawrence J. S., Bland-Hawthorn J., Bryant J. J., Fogarty L., Richards S., Goodwin M., Farrell T. et al, 2012, MNRAS, 421, 872
Dalla Vecchia C., Schaye J., 2012, MNRAS, 426, 140
D'Eugenio F., Houghton R. C. W., Davies R. L., Dalla Bontà E., 2013, MNRAS, 429, 1258
Di Matteo P., Jog C. J., Lehnert M. D., Combes F., Semelin B., 2009, A&A, 501, L9
Dolag K., Borgani S., Murante G., Springel V., 2009, MNRAS, 399, 497
Dubois Y., Peirani S., Pichon C., Devriendt J., Gavazzi R., Welker C., Volonteri M., 2016, MNRAS, 463, 3948
Dubois Y., Pichon C., Welker C., Le Borgne D., Devriendt J., Laigle C., Codis S., Pogosyan D. et al, 2014, MNRAS, 444, 1453
Dutton A. A., Bosch F. C. V. D., Faber S. M., Simard L., Kassin S. A., Koo D. C., Bundy K., Huang J. et al, 2011, MNRAS, 410, 1660
El-Badry K., Quataert E., Wetzel A., Hopkins P. F., Weisz D. R., Chan T. K., Fitts A., Boylan-Kolchin M. et al, 2018, MNRAS, 473, 1930
Emsellem E., Cappellari M., Krajnović D., Alatalo K., Blitz L., Bois M., Bournaud F., Bureau M. et al, 2011, MNRAS, 414, 888
Emsellem E., Cappellari M., Krajnović D., van de Ven G., Bacon R., Bureau M., Davies R. L., de Zeeuw P. T. et al, 2007, MNRAS, 379, 401
Furlong M., Bower R. G., Theuns T., Schaye J., Crain R. A., Schaller M., Dalla Vecchia C., Frenk C. S. et al, 2015, MNRAS, 450, 4486
Genel S., Vogelsberger M., Springel V., Sijacki D., Nelson D., Snyder G., Rodriguez-Gomez V., Torrey P. et al, 2014, MNRAS, 445, 175
Greene J. E., Leauthaud A., Emsellem E., Ge J., Arag'on-Salamanca A., Greco J. P., Lin Y.-T., Mao S. et al, 2017, ArXiv e-prints
Guo Q., Gonzalez-Perez V., Guo Q., Schaller M., Furlong M., Bower R. G., Cole S., Crain R. A. et al, 2015, ArXiv:1512.00015
Houghton R. C. W., Davies R. L., D'Eugenio F., Scott N., Thatte N., Clarke F., Tecza M., Salter G. S. et al, 2013, MNRAS, 436, 19
Jesseit R., Cappellari M., Naab T., Emsellem E., Burkert A., 2009, MNRAS, 397, 1202
Jiang L., Helly J. C., Cole S., Frenk C. S., 2014, MNRAS, 440, 2115
Johansson P. H., Naab T., Burkert A., 2009, ApJ, 690, 802
Katsianis A., Blanc G., Lagos C. P., Tejos N., Bower R. G., Alavi A., Gonzalez V., Theuns T. et al, 2017, MNRAS, 472, 919
Krajnović D., Alatalo K., Blitz L., Bois M., Bournaud F., Bureau M., Cappellari M., Davies R. L. et al, 2013, MNRAS, 432, 1768
Krajnović D., Cappellari M., de Zeeuw P. T., Copin Y., 2006, MNRAS, 366, 787
Kregel M., van der Kruit P. C., de Grijs R., 2002, MNRAS, 334, 646
Lagos C. d. P., Crain R. A., Schaye J., Furlong M., Frenk C. S., Bower R. G., Schaller M., Theuns T. et al, 2015, MNRAS, 452, 3815
Lagos C. d. P., Stevens A. R. H., Bower R. G., Davis T. A., Contreras S., Padilla N. D., Obreschkow D., Croton D. et al, 2018, MNRAS, 473, 4956
Lagos C. d. P., Theuns T., Schaye J., Furlong M., Bower R. G., Schaller M., Crain R. A., Trayford J. W. et al, 2016, MNRAS, 459, 2632
Lagos C. d. P., Theuns T., Stevens A. R. H., Cortese L., Padilla N. D., Davis T. A., Contreras S., Croton D., 2017, MNRAS, 464, 3850
Li H., Mao S., Emsellem E., Xu D., Springel V., Krajnović D., 2018, MNRAS, 473, 1489
Lotz J. M., Jonsson P., Cox T. J., Primack J. R., 2010, MNRAS, 404, 590
Ma C.-P., Greene J. E., McConnell N., Janish R., Blakeslee J. P., Thomas J., Murphy J. D., 2014, ApJ, 795, 158
McAlpine S., Helly J. C., Schaller M., Trayford J. W., Qu Y., Furlong M., Bower R. G., Crain R. A. et al, 2015, ArXiv:1510.01320
Mo H. J., Mao S., White S. D. M., 1998, MNRAS, 295, 319
Moreno J., Torrey P., Ellison S. L., Patton D. R., Bluck A. F. L., Bansal G., Hernquist L., 2015, MNRAS, 448, 1107
Moster B. P., Macciò A. V., Somerville R. S., Naab T., Cox T. J., 2011, MNRAS, 415, 3750
Naab T., Oser L., Emsellem E., Cappellari M., Krajnović D., McDermid R. M., Alatalo K., Bayet E. et al, 2014, MNRAS, 444, 3357
Nelson D., Pillepich A., Springel V., Weinberger R., Hernquist L., Pakmor R., Genel S., Torrey P. et al, 2017, ArXiv e-prints
Oliva-Altamirano P., Brough S., Tran K.-V., Jimmy, Miller C., Bremer M. N., Phillipps S., Sharp R. et al, 2017, AJ, 153, 89
Pasquali A., van den Bosch F. C., Rix H.-W., 2007, ApJ, 664, 738
Peirani S., Crockett R. M., Geen S., Khochfar S., Kaviraj S., Silk J., 2010, MNRAS, 405, 2327
Peng Y.-j., Lilly S. J., Kovač K., Bolzonella M., Pozzetti L., Renzini A., Zamorani G., Ilbert O. et al, 2010, ApJ, 721, 193
Penoyre Z., Moster B. P., Sijacki D., Genel S., 2017, MNRAS, 468, 3883
Pillepich A., Springel V., Nelson D., Genel S., Naiman J., Pakmor R., Hernquist L., Torrey P. et al, 2017, ArXiv e-prints

Planck Collaboration, 2014, A&A, 571, A16
Qu Y., Helly J. C., Bower R. G., Theuns T., Crain R. A., Frenk C. S., Furlong M., McAlpine S. et al, 2017, MNRAS, 464, 1659
Rahmati A., Pawlik A. H., Raicevic M., Schaye J., 2013, MNRAS, 430, 2427
Robertson B., Bullock J. S., Cox T. J., Di Matteo T., Hernquist L., Springel V., Yoshida N., 2006, ApJ, 645, 986
Robotham A. S. G., Norberg P., Driver S. P., Baldry I. K., Bamford S. P., Hopkins A. M., Liske J., Loveday J. et al, 2011, MNRAS, 416, 2640
Rosas-Guevara Y. M., Bower R. G., Schaye J., Furlong M., Frenk C. S., Booth C. M., Crain R. A., Dalla Vecchia C. et al, 2015, MNRAS, 454, 1038
Sánchez S. F., Kennicutt R. C., Gil de Paz A., van de Ven G., Vílchez J. M., Wisotzki L., Walcher C. J., Mast D. et al, 2012, A&A, 538, A8
Saulder C., van Kampen E., Chilingarian I. V., Mieske S., Zeilinger W. W., 2016, A&A, 596, A14
Schaller M., Dalla Vecchia C., Schaye J., Bower R. G., Theuns T., Crain R. A., Furlong M., McCarthy I. G., 2015, MNRAS, 454, 2277
Schaye J., Crain R. A., Bower R. G., Furlong M., Schaller M., Theuns T., Dalla Vecchia C., Frenk C. S. et al, 2015, MNRAS, 446, 521
Schaye J., Dalla Vecchia C., 2008, MNRAS, 383, 1210
Snyder G. F., Torrey P., Lotz J. M., Genel S., McBride C. K., Vogelsberger M., Pillepich A., Nelson D. et al, 2015, MNRAS, 454, 1886
Sparre M., Springel V., 2016, MNRAS, 462, 2418
—, 2017, MNRAS, 470, 3946
Springel V., 2000, MNRAS, 312, 859
—, 2005, MNRAS, 364, 1105
Springel V., White S. D. M., Tormen G., Kauffmann G., 2001, MNRAS, 328, 726
Swinbank A. M., Harrison C. M., Trayford J., Schaller M., Smail I., Schaye J., Theuns T., Smit R. et al, 2017, MNRAS
Trayford J. W., Theuns T., Bower R. G., Crain R. A., Lagos C. d. P., Schaller M., Schaye J., 2016, MNRAS, 460, 3925
Trayford J. W., Theuns T., Bower R. G., Schaye J., Furlong M., Schaller M., Frenk C. S., Crain R. A. et al, 2015, MNRAS, 452, 2879
van de Sande J., Bland-Hawthorn J., Fogarty L. M. R., Cortese L., d'Eugenio F., Croom S. M., Scott N., Allen J. T. et al, 2017, ApJ, 835, 104
Veale M., Ma C.-P., Greene J. E., Thomas J., Blakeslee J., McConnell N., Walsh J., Ito J., 2017a, ArXiv e-prints
Veale M., Ma C.-P., Thomas J., Greene J. E., McConnell N. J., Walsh J., Ito J., Blakeslee J. P. et al, 2017b, MNRAS, 464, 356
Vogelsberger M., Genel S., Springel V., Torrey P., Sijacki D., Xu D., Snyder G., Bird S. et al, 2014, Nature, 509, 177
Welker C., Dubois Y., Pichon C., Devriendt J., Chisari E. N., 2015, ArXiv:1512.00400
Wiersma R. P. C., Schaye J., Smith B. D., 2009a, MNRAS, 393, 99
Wiersma R. P. C., Schaye J., Theuns T., Dalla Vecchia C., Tornatore L., 2009b, MNRAS, 399, 574
Yang X., Mo H. J., van den Bosch F. C., Pasquali A., Li C., Barden M., 2007, ApJ, 671, 153
Zavala J., Frenk C. S., Bower R., Schaye J., Theuns T., Crain R. A., Trayford J. W., Schaller M. et al, 2016, MNRAS, 460, 4466

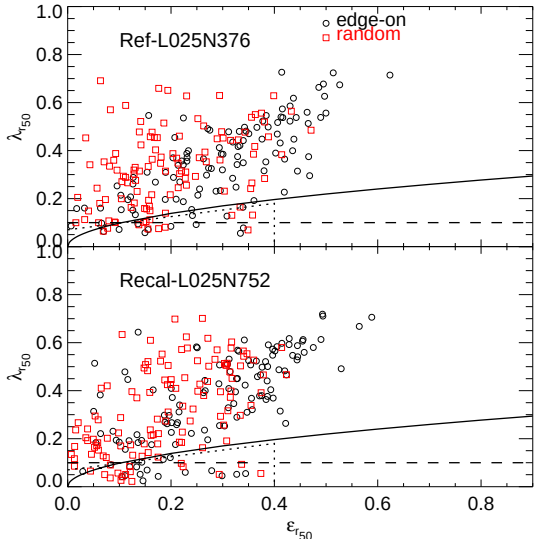

Figure A1. $\lambda_{\rm r50}$ as a function of ellipticity for galaxies in the Ref-L025N0376 (top panel) and Recal-L025N0752 (bottom panel) simulations that have $M_{\rm stars} \geqslant 5 \times 10^9\,{\rm M}_\odot$ at $z = 0$. Circles and squares show galaxies seen edge-on and randomly, respectively. The three lines correspond to different classifications of slow rotations, and are as in Fig. 3.

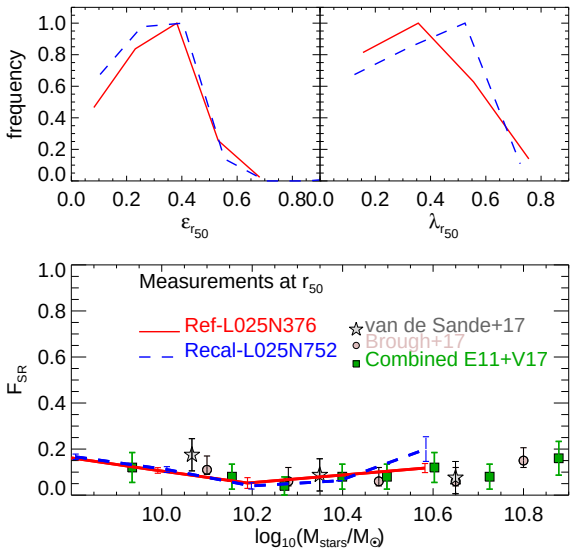

Figure A2. *Top panel:* Distribution of edge-on $\lambda_{\rm r50}$ and ϵ for the galaxies in Fig. A1. Solid and dashed lines correspond to the Ref-L025N0376 and Recal-L025N0752 simulations, respectively. *Bottom panel:* $F_{\rm SR}$ using the Cappellari (2016) criterion as a function of stellar mass in the Ref-L025N0376 (solid line) and Recal-L025N0752 (dashed line) simulations. Error bars correspond to 1σ calculated with 10 jackknife resamplings in individual mass bins.

APPENDIX A: CONVERGENCE TESTS

A1 Resolution convergence

We present convergence tests for the ellipticity and $\lambda_{\rm R}$ measurements performed on galaxies with $M_{\rm stars} \geqslant 5 \times 10^9\,{\rm M}_\odot$ at r_{50}. The stellar mass limit above was motivated by Lagos et al. (2017) as the stellar mass above which the stellar specific angular momentum of galaxies measured at $r \geqslant r_{50}$ converges. For our convergence test we use the run referred to as Recal-L025N0752 in S15, which corresponds to a volume of length $L = 25$ cMpc and with 2×752^3 particles, and that adopts the same sub-grid physics as the reference simulation used in this work (Ref-L100N1504 and Ref-L050N752; see Table 1), but has parameters adjusted to fit the stellar mass function at $z = 0$. This is referred to as 'weak convergence' test in S15. To allow for a fair comparison, we use the Ref-L025N0376, which has the same resolution, subgrid physics and parameters as the simulations in Table 1, but with a box of length $L = 25$ cMpc.

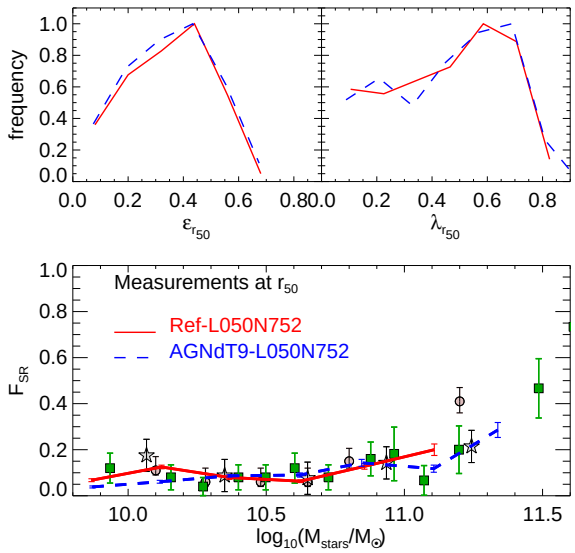

Figure A3. As in Fig. A2 but for the Ref-L050N0752 and the AGNdT9-L050N0752 simulations.

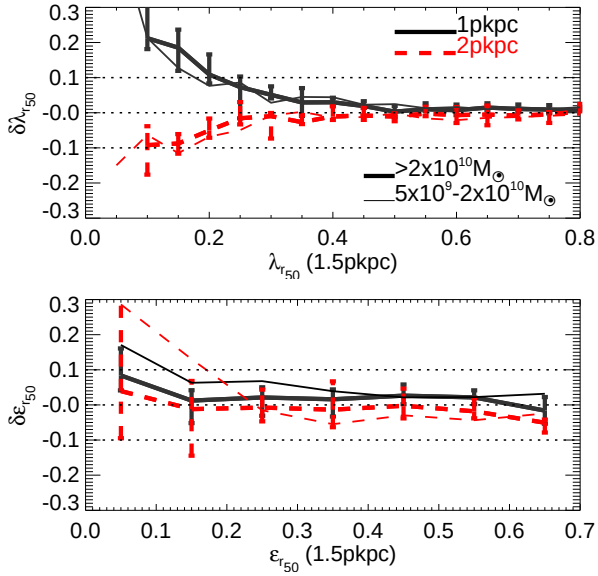

Figure A4. The fractional variation of $\lambda_{\rm r50}$ (top panel) and $\epsilon_{\rm r50}$ (bottom panel) as a function of these two quantities using bins of 1 and 2 pkpc, as labelled (see Eq. A1 for a definition of the fractional variation). Lines and error bars show the median and $25^{\rm th}-75^{\rm th}$ percentile ranges. **For clarity errorbars are shown only for one mass bin.** In this test we use the Ref-L050N0752 simulation and show galaxies at $z=0$ **in two stellar mass bins,** $5\times10^9\,{\rm M}_\odot < {\rm M}_{\rm stars} < 2\times10^{10}\,{\rm M}_\odot$ **(thin lines) and** $M_{\rm stars}\geqslant 2\times10^{10}\,{\rm M}_\odot$ **(thick lines).**

Fig. A1 shows $\lambda_{\rm r50}$ as a function of ellipticity for galaxies in the Ref-L025N0376 and Recal-L025N0752 simulations. Both simulations occupy a similar parameter space, though with the Recal-L025N0752 simulation populating a bit more the high $\lambda_{\rm r50}$ area. This is better seen in the top panel of Fig. A2, which shows the distribution of $\lambda_{\rm r50}$ and ellipticity, measured adopting an edge-on orientation, for galaxies with $M_{\rm stars}\geqslant 5\times10^9\,{\rm M}_\odot$ in both simulations. The simulations produce ϵ distributions that are very similar, but in $\lambda_{\rm r50}$ we see a tendency of the Recal-L025N0752 simulation to produce more galaxies with high $\lambda_{\rm r50}$ (i.e. the peak of the $\lambda_{\rm r50}$ distribution shifts slightly towards higher $\lambda_{\rm r50}$ in the Recal-L025N075 simulation). Despite these differences, the fraction of slow rotators (bottom panel of Fig. A2) agrees very well, within the error bars. Since in this paper we are mainly concerned about the latter, we conclude that there is good convergence of the results presented throughout this manuscript.

A2 Reference vs. AGNdT9 model

The model adopted in HYDRANGEA is the same as in the Reference EAGLE runs, except for the temperature to which gas particles are heated by AGN. The reference EAGLE model adopts $\Delta T_{\rm AGN}=10^{8.5}$ K and $C_{\rm visc}=2\pi$, while HYDRANGEA adopts $\Delta T_{\rm AGN}=10^9$K and $C_{\rm visc}=2\pi\times10^2$, with the purpose of decreasing the gas fraction is large groups and clusters. As part of EAGLE, this model was run in the $50\,({\rm cMpc})^3$ box, and so here we compare these two models, fixing the box size, number of particles and initial conditions. We refer to these models as Ref-L050N0752 and the AGNdT9-L050N0752.

Fig. A3 shows a comparison of $\epsilon_{\rm r50}$ and $\lambda_{\rm r50}$ in the Ref-L050N0752 and the AGNdT9-L050N0752 (top panel) and the fraction of slow rotators as a function of stellar mass at $z=0$ (bottom panel). Both simulations show a similar $\epsilon_{\rm r50}$ and $\lambda_{\rm r50}$ distributions, and produce a similar $F_{\rm SR}-M_{\rm stellar}$ relation (bottom panel of Fig. A3), except at the highest mass bin. where the AGNdT9-L050N0752 model tends to have a lower $F_{\rm SR}$ compared to the Ref-L050N0752 model.

A3 Convergence of kinematic measurements

To create the r-band luminosity-weighted mock IFU-like cubes for each simulated galaxy we bin the 2D projected r-band luminosity map as described in § 2.1. The chosen bin for the analysis of this paper is 1.5 pkpc. Here we analyse the impact of this bin on the quantities of interest $\lambda_{\rm r50}$ and $\epsilon_{\rm r50}$. For this analysis, we use the Ref-L050N0752 simulation and select all galaxies that $z=0$ have $M_{\rm stars}\geqslant 5\times10^9\,{\rm M}_\odot$. We recompute all kinematic quantities but this time using bins of 1 and 2 pkpc. We define the fractional variation δ of a kinematic quantity x in terms of the value obtained when we adopt a bin of 1.5 pkpc,

$$\delta x({\rm bin})=\frac{[{\rm x(bin)}-{\rm x(1.5\ pkpc)}]}{{\rm x(1.5\ pkpc)}}. \quad ({\rm A1})$$

In Fig. A4 we show the impact the adopted bin has on the measurements of $\epsilon_{\rm r50}$ and $\lambda_{\rm r50}$ in two bins of stellar mass. Adopting a smaller bin, closer to the softening length (see Table 1), drives significant deviations in $\lambda_{\rm r50}$ at low values of $\lambda_{\rm r50}$, while adopting a larger bin does not have much of an impact. This is expected as choosing smaller bins, too close to the resolution limit, imply a much smaller number of particles per bin, which can produce significant errors in the determination of the kinematic parameters. **We find that the two bins of stellar mass reach similar results.** $\epsilon_{\rm r50}$ is barely affected by the chosen bin, as expected, since what matters for ϵ is that the r-band luminosity map is well converged, which is much easier than converging on the velocity profile of individual bins. **The only exception is at low stellar masses when we choose a bin of 2 pkpc. This is not surprising as the sizes of these galaxies are relatively small (average $r_{50}\approx5$ pkpc), and thus the bin has to be small enough as to sample the mass distri-**

bution within r_{50}. Our results show that choosing a bin of 1 pkpc is not appropriate for a simulation of the resolution of EAGLE, while choosing 1.5 or 2 pkpc has little impact on the kinematic measurements, implying good convergence. $\epsilon_{r_{50}}$ and $\lambda_{r_{50}}$ are converged to better than 7% for our adopted bin.